Two orders of magnitude reduction in silicon membrane thermal conductivity by resonance hybridizations

Hossein Honarvar and Mahmoud I. Hussein

Phys. Rev. B **97**, 195413 — Published 9 May 2018

DOI: 10.1103/PhysRevB.97.195413

Two Orders of Magnitude Reduction in Silicon Membrane Thermal Conductivity by Resonance Hybridizations

Hossein Honarvar and Mahmoud I. Hussein*
Ann and H.J. Smead Department of Aerospace Engineering Sciences, University of Colorado Boulder, Boulder, Colorado 80309, USA
(Dated: April 16, 2018)

The thermal conductivity of a freestanding single-crystal silicon membrane may be reduced significantly by attaching nanoscale pillars on one or both surfaces. Atomic resonances of the nanopillars form vibrons that intrinsically couple with the base membrane phonons causing mode hybridization and flattening at each coupling location in the phonon band structure. This in turn causes group velocity reductions of existing phonons, in addition to introducing new modes that are localized and do not transport energy. The nanopillars also reduce the phonon lifetimes at and around the hybridization zones. These three effects, which in principle may be tuned to take place across silicon's full spectrum, lead to a lowering of the in-plane thermal conductivity in the base membrane. Using equilibrium molecular dynamics simulations, and utilizing the concept of vibrons compensation, we report a staggering two orders of magnitude reduction in the thermal conductivity at room temperature by this mechanism. Specifically, a reduction of a factor of 130 is demonstrated for a roughly 10-nm thick pillared membrane compared to a corresponding unpillared membrane. This amounts to a record reduction of a factor of 481 compared to bulk crystalline silicon and nearly a factor of 2 compared to bulk amorphous silicon. These results are obtained while providing a path for preserving performance with upscaling.

I. INTRODUCTION

The emerging field of *phononics* seeks to elucidate the nature of phonon dynamics in both conventional and artificially structured materials and use this knowledge to extend the boundaries of physical response at either the material or structural/device level or both [1]. The field targets primarily acoustic, elastic, and/or thermal properties and usually involves the investigation and utilization of complex wave mechanisms encompassing one or more of a diverse range of phenomena such as dispersion, resonances, dissipation, and nonlinear interactions [2].

In the subfield of *nanophononics*, an intensely active area of research is the search for strategies for reducing a material's thermal conductivity [3], and in particular strategies that would not deteriorate the electrical properties [4].[5] Attaining a low value of the thermal conductivity k and simultaneously high values of the electrical conductivity σ and the Seebeck coefficient S is strongly desired in thermoelectric materials−materials that convert heat to electric energy, or, conversely, use electricity to provide heating or cooling [6]. The performance of a thermoelectric material is measured by a figure of merit defined as $ZT = (\sigma S^2/k)T$, where T is the absolute temperature and k is the sum of a lattice component k_l and an electrical component k_e [7].

Over the past few decades, a large research effort has focused on semiconductors where $k_\mathrm{l} \gg k_\mathrm{e}$. The prevailing approach to increasing ZT in this class of materials is to introduce small and closely spaced features (such as holes, particles, and/or interfaces) within the internal domain of the material to scatter the heat-carrying phonons and consequently reduce the lattice thermal conductivity, e.g., see Ref. [8]. This strategy, however, faces the challenge that the scatterers are also likely to impede the transfer of electrons and thus negate any possibility of substantial increase in ZT. Another approach is the use of superlattices [9] or nanophononic crystals [4,10,11] where the aim is to use Bragg scattering to open up phonon band gaps and reduce the group velocities by flattening the dispersion curves. A practical disadvantage to this route, however, is that the surfaces of the periodic features, e.g., the layers, holes or inclusions, need to be considerably smooth to preserve the phase information required for the Bragg effects to take place−especially when the features are of relatively large sizes compared to the phonon wavelengths [12]. An even stronger drawback is that the degree and intensity of group-velocity reduction is rather limited and cannot be enhanced beyond what the available Bragg interference patterns can provide. One other promising avenue is through dimensionality reduction, e.g., considering thermal transport along a nanowire [13]. This introduces phonon confinement and strong phonon scattering at the free surfaces, especially when roughened or oxidized [14]. Yet this approach too, when used alone, is relatively limited in its capacity to lowering the thermal conductivity without excessive reduction in the size of the smallest dimension.

In our group at CU-Boulder, we have been investigating a fundamentally different paradigm for increasing ZT. Instead of depending on boundary-type scattering (internal or external), Bragg interferences, and/or phonon confinement as leading mechanisms for lowering k_l, we employ local resonances [15–17]. In this concept, termed *nanophononic metamaterial* (NPM), nanoscale resonating substructures are intrinsically introduced to a conventional semiconducting material which acts as the prime thermoelectric medium. The purpose of these substructures is not to generate subwavelength band gaps or create negative long-wave effective properties as is

the case for locally resonant electromagnetic [18], acoustic [19], and elastic [20] metamaterials, but to reduce the phonon group velocities of the underlying semiconducting material, as well as populate it with a large number of localized modes, in order to significantly reduce its thermal conductivity.[21] The substructure resonances may be designed to couple with heat-carrying phonon modes belonging to all or most of the dispersion branches across the full spectrum of the host medium.[22] This atomic-scale coupling mechanism gives rise to a *resonance hybridization* between pairs of the wavenumber-independent vibration modes of the local substructure (vibrons) and wavenumber-dependent wave modes of the host medium (phonons). The stronger the couplings, the sharper the curve flattenings, which in turn implies larger reductions in the group velocities and stronger mode localizations within the substructures. The phonon lifetimes also drop at the coupling locations in the phonon band structure, which provides yet further reduction in the thermal conductivity. In the limit, the number of hybridizing resonances is three times the number of atoms in a unit nanoresonator.

A candidate configuration of an NPM consists of an array, or a forest, of silicon nanopillars distributed on the surface(s) of a freestanding silicon membrane with no interior scatterers [15–17]. Here the nanopillars act as the resonating substructures. Since the nanopillars are located external to the main body of the membrane, the electronic band structure is only mildly affected and the scattering of electrons occurs only near the membrane surfaces and not in the interior. Compared to all conventional phonon scattering-based approaches (where the scatterers are in the main body of the transport medium), this new route therefore provides the unique advantage of practically decoupling the lattice thermal conductivity from the Seebeck coefficient and the electrical conductivity—which is essential to creating significant improvements in ZT. And compared to superlattices and nanophononic crystals, an NPM in general has two advantages: (i) the structural features do not need to be periodic or smooth (because the resonance hybridization phenomenon is independent of periodicity and robust to perturbations in phase), and (ii) the intensity of

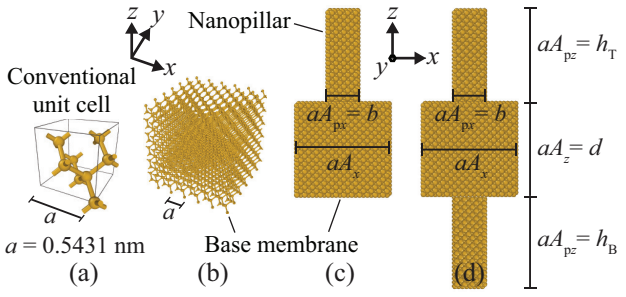

FIG. 1. (a) Conventional 8-atom unit cell for silicon and unit cells for a (b) uniform membrane, (c) single-pillared NPM, and (d) double-pillared NPM. In (b), (c) and (d), the top and bottom surfaces are free.

group-velocity reductions, with the added benefit of introduction of localized modes and targeted phonon lifetime reductions, may be continuously enhanced by simply increasing the size of the nanoresonators [17,23].[24] Finally, a nanopillared freestanding membrane naturally exhibits dimensionality reduction (compared to the bulk form). Therefore, the powerful rewards of resonance hybridizations are gained over and above the benefits of phonon confinement and/or surface roughness (as well as the benefits to the electrical properties [25]). In light of these impressive characteristics that are unprecedented in thermal transport, the NPM concept in the form of a nanopillared membrane is poised to enable thermoelectric energy conversion at record high performance, while using a low-cost and practical base material like silicon.

In a recent study involving nanopillars on one surface, it was shown that the performance of this membrane-based NPM configuration is highly dependent on: (i) the relative volumetric size of the nanopillar with respect to the base membrane within the unit cell (this quantity is denoted V_r and is equal to $\mathrm{DOF}_\mathrm{Pillar}/\mathrm{DOF}_\mathrm{Base}$ where $\mathrm{DOF}_\mathrm{Pillar}$ and $\mathrm{DOF}_\mathrm{Base}$ denote nanopillar(s) and base membrane number of degrees of freedom, respectively) and (ii) the overall size of the unit cell (including both the base membrane and nanopillar portions) [17]. While the first dependency provides a controllable design parameter (which is an advantage as mentioned above), the second was shown to pose a challenge because unless V_r is relatively high to start with, the extent of the thermal conductivity reduction will deteriorate as the overall unit-cell size is proportionally scaled up [17]. In this paper, we explore the possibility of "compensating" this loss in performance by increasing the nanopillar size at a higher rate than the base membrane as we progressively examine larger unit cells. By following this path, we demonstrate that it is possible to even reverse the trend and, remarkably, achieve exceedingly high performance with upscaling. Throughout the paper, this *compensatory effect* is utilized and analyzed thoroughly in the context the underlying thermal conductivity reduction mechanisms. Towards the end of our investigation, we highlight the potential thermoelectric performance of NPMs by providing ZT projections and contrasting the reduced values of the thermal conductivity with that of the extreme case of bulk amorphous silicon.

II. CHARACTERISTICS OF NPM PHONONS AND VIBRONS

We investigate two prime freestanding NPM configurations: a membrane with nanopillars (i) on one surface, and (ii) on each of the surfaces. In all cases, both base membrane and nanopillar(s) are made of defect-free single-crystal silicon. Figure 1 displays the unit cells of these two configurations as well as the structure of a conventional cell (CC) and a unit cell of a corresponding

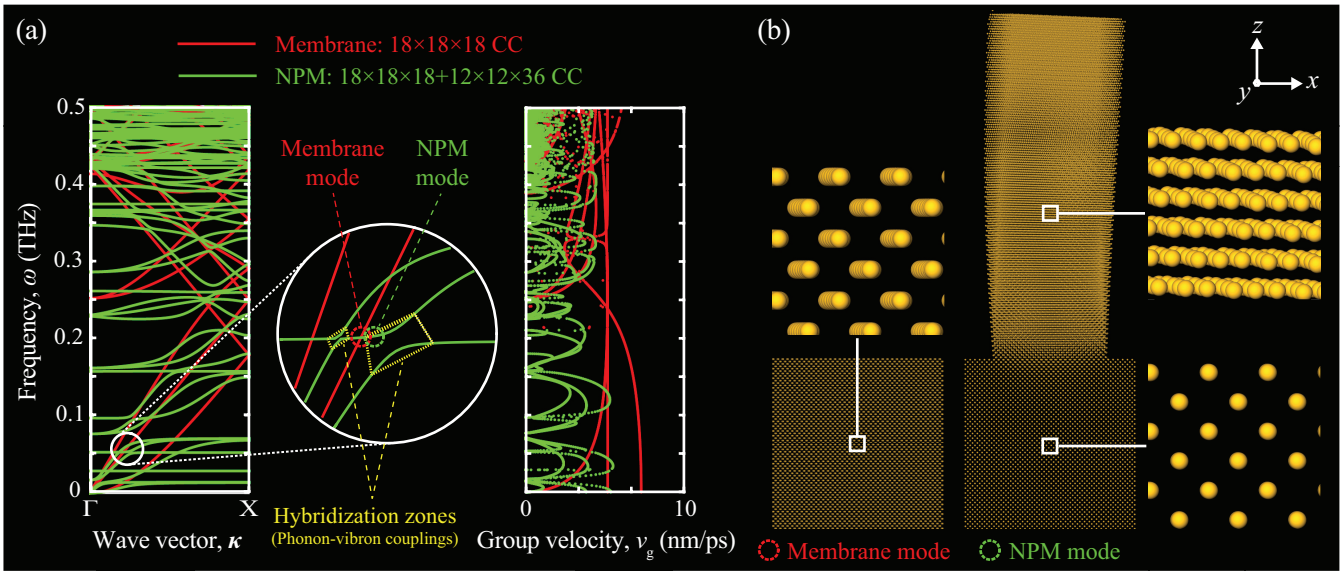

FIG. 2. Illustration of the resonance hybridization phenomenon from a lattice dynamics perspective. (a) Phonon band structure and group velocity distribution of a silicon membrane with (green) or without (red) silicon nanopillars standing on one surface. (b) Uniform membrane atomic displacements for a heat carrying phonon mode in the acoustic regime contrasted to NPM atomic displacements of the same mode upon resonance hybridization. Significant motion within the uniform membrane is seen. In contrast, the atomic displacements of the NPM hybridized mode reveals localized nanopillar motion and almost 'thermal silence' in the base membrane portion. In (a), a zoom-in is provided for two hybridization zones including the one illustrated in (b). A magnification factor of 2000 is applied to the atomic displacements in the mode-shape images.

uniform (unpillared) membrane. The geometry of a membrane with nanopillars on each surface is represented as $aA_x \times aA_y \times d + b \times b \times h_{\mathrm{T}} + b \times b \times h_{\mathrm{B}}$ which may be converted to CC by dividing each dimension by a. Each of the last two terms in this representation is dropped as needed when representing an unpillared surface. All geometric parameters are pictorially defined in Fig. 1. Unless explicitly specified, in all our analyses room temperature at $T = 300$ K is assumed and the Stillinger-Weber empirical potential is used to represent the interatomic interactions [26].

A. Band structure and density of states

As we have described in Section I, the key mechanism in an NPM is the coupling between phonons whose motion is confined to the in-plane directions within the base membrane and vibrons whose motion is limited primarily to the domain of each nanopillar. The former may be viewed as traveling waves propagating in an infinite medium, and the latter may be viewed as standing waves taking shape in finite structures branching out orthogonally from this infinite medium. Our interest is in the steady-state characteristics of these two types of waves as well as the manner by which they linearly interact across the full spectrum. Nonlinear interaction between these waves is also possible, and in fact takes place, but is not the prime focus in this investigation.

Figure 2 provides a demonstration of the linear interaction between phonons and vibrons, i.e., the resonance hybridization phenomenon, as manifested in the phonon band structure, group-velocity distributions, and associated mode shapes. For this purpose, we consider an $18\times18\times18+12\times12\times36$ CC NPM unit cell (consisting of 88128 atoms) and use the reduced Bloch mode expansion (RBME) technique [27] to solve the corresponding eigenvalue problem over the 0-0.5 THz range (see Appendix A for RBME implementation details). The effects of the phonon-vibron mode coupling phenomenon are clearly displayed. Figure 2a shows the resonance hybridizations in the quasiharmonic frequency versus wavenumber dispersion diagram and the corresponding reduction in the group velocities across the entire frequency range plotted (the same effect extends throughout the entire spectrum). Reduction in phonon group velocities directly implies reduction in the thermal conductivity. Figure 2b focuses on a particular mode in the band structure and displays the unit-cell mode shape without and with resonance hybridization. The localization of the atomic motion solely in the nanopillar region represents a case of extreme localization of energy—metaphorically as if the nanoresonator is acting like a "phonon siphon" sucking the energy from the base membrane and retaining it in the nanopillar portion. This phenomenon is significant because the nanopillar portion contributes to the unit-cell's overall heat capacity, yet these localized modes appear in the band structure as horizontal (or almost horizontal) lines and thus exhibit zero (or-near-zero) group velocities.

In Fig. 3, we show the effects of the size and geometry

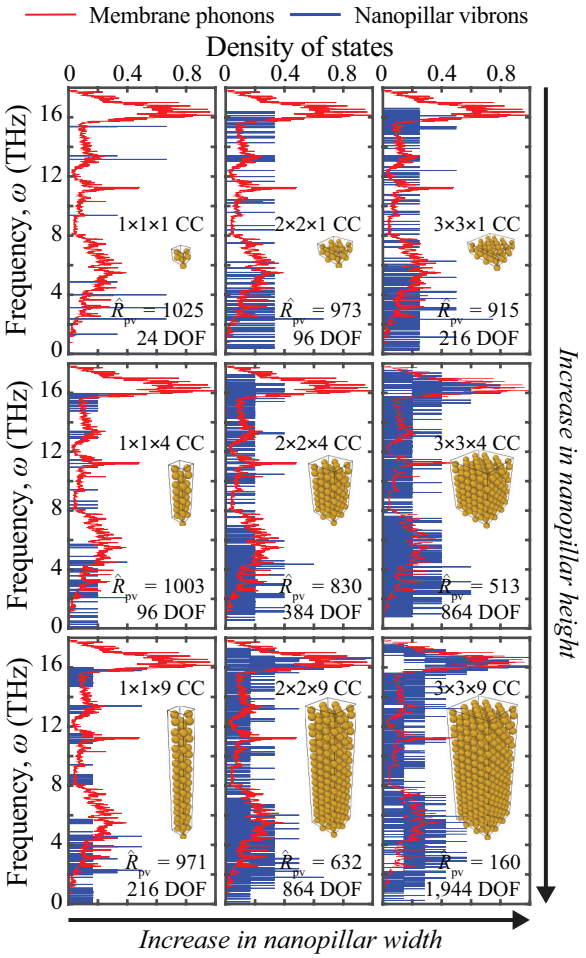

FIG. 3. Direct correlation between silicon membrane phonons DOS (considering a $6 \times 6 \times 6$ CC membrane) and silicon nanopillar vibrons DOS for various nanopillar side lengths and heights. The latter quantities are obtained by considering the nanopillar as an independent nanostructure with free boundary conditions. All quantities are normalized with respect to their maximum values.

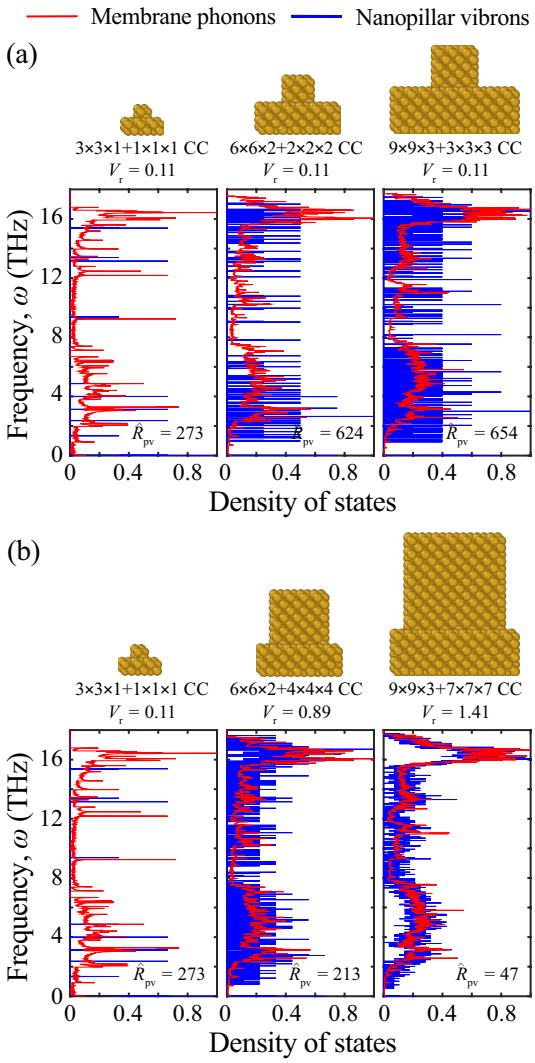

FIG. 4. Demonstration of phonon-vibron conformity as a function of unit-cell size and V_r. Relative distributions of the phonons and vibrons DOS are shown for three NPMs whose V_r values are (a) kept constant and (b) increased as the overall unit-cell size grows. The leftmost NPM configuration has a $3 \times 3 \times 1$ CC membrane and a $1 \times 1 \times 1$ CC nanopillar. The vibron DOS are obtained by considering the nanopillar as an independent nanostructure with free boundary conditions. All quantities are normalized with respect to their maximum values. Increasing the size of the nanopillar at a higher rate than the size of the membrane leads to higher phonon-vibron conformity, which corresponds to lower values of $\hat{R}_{\rm pv}$ and a more intense resonance hybridizations effect.

of a nanopillar on the distribution of the vibrons density of states (DOS) and how it correlates with that of the phonons DOS of the underlying base membrane. It is observed that for the same number of atoms, a wider nanopillar provides a more spread-out local resonances spectrum than a tall nanopillar. The higher the vibrons densities and the more conforming to the phonons distribution, the more effective is the resonance hybridizations phenomenon—especially at low frequencies down to the limit of existing wavelengths (see Section II B). For the largest nanopillar, we clearly see a near-perfect conformity between the two distributions owing to the fact that both membrane and nanopillar are made of the same material. Recalling from Fig. 2, mode localizations take place at each region in the spectrum where phonon dispersion curves and horizontal vibron resonance lines hybridize. Unlike Anderson localization [28], the localization phenomenon in the present system does not require disorder; the position, spatial extent, and spectral intensity of the localizations are controlled by the location, size, and geometry of the unit nanoresonator.

The notion of conformity we refer to in our discussion of Fig. 3 may be quantified. Conveniently, we introduce a metric to represent its converse, namely, the *nonconformity factor* $\hat{R}_{\rm pv}$, which we define as

$$\hat{R}_{\rm pv} = \|R_{\rm pv} - R_{\rm pp}\|, \tag{1}$$

where $R_{\rm pv}$ is the cross-correlation between the phonons and the vibrons DOS, $R_{\rm pp}$ is the auto-correlation of the

phonons DOS, and $\|.\|$ denotes the double norm. The reader may refer to Ref. [29] for the definitions of correlation functions. The nonconformity factor varies between 0 (perfect conformity) and ∞ (no conformity). Consistent with our previous remarks, we observe that an NPM with a wide and short nanopillar indeed has a lower nonconformity factor (i.e., has a higher level of conformity) compared to an NPM with a narrow and tall nanopillar and the same total number of DOF.

1. *Effect of vibrons compensation on phonon-vibron conformity*

In Fig. 4, we take this analysis further and examine how the overall size of the NPM affects the phonons and vibrons DOS distributions, separately and with respect to each other. We see in Fig. 4a that as the sizes of the membrane and nanopillar portions are increased at an identical rate, the value of the nonconformity factor rises. On the other hand, we observe in Fig. 4b that when the size of the nanopillar portion is increased at a higher rate compared to the membrane portion, this value decreases, i.e., the degree of conformity intensifies. The former scenario corresponds to the set of cases considered in Ref. [17]. On the other hand, the latter scenario represents a design pathway that creates compensation, as described in Section I. For compensation to be realized, nanopillar vibrons are added at a higher rate than membrane phonons as the overall size of the unit cell examined is increased. The outcome is that not only (1) the phonon band structure gets enriched with a higher vibrons-to-phonons ratio, but also (2) the level of conformity between the phonon and vibrons DOS distributions gets significantly enhanced.

2. *Effect of vibrons compensation on group-velocity and mode-weight-factor reductions*

The degree of phonon-vibron conformity has significant effects on all three mechanisms for thermal conductivity reduction. Considering the reduction in group velocities and the introduction of nanopillar localized modes, this is demonstrated in Fig. 5 where we again consider the three NPM configurations shown in Fig. 4b which feature vibrons compensation as the membrane thickness is increased. In Fig. 5a, we show the group velocity frequency distribution across the full spectrum for each NPM and its corresponding uniform membrane with the same base membrane thickness. In order to quantify the reduction in the group velocities across the full spectrum, the average group-velocity ratio is computed and defined as $G_\mathrm{r} = G_\mathrm{NPM}/G_\mathrm{memb}$, where the average group velocity G is calculated for each system (NPM or uniform membrane) by

$$G = [1/(n_\kappa n_m)] \sum_\kappa^{n_\kappa} \sum_m^{n_m} v_\mathrm{g}(\kappa, m), \qquad (2)$$

where v_g is the group velocity, n_κ is the number of wavenumber points considered, $n_m = 3N$ is the total number of modes for an N-atom unit cell, κ is the wavenumber (scalar component of wave vector $\boldsymbol{\kappa}$), and m denotes the branch number in the dispersion diagram; see Ref. [17] for additional analysis on the influence of the nanopillars on the group velocity characteristics. Clearly, we see that G_r drops as the size increases with a higher growth rate in the nanopillar portion, which is a manifestation of the compensatory effect. To similarly investigate the impact of the compensatory effect on the mode localizations, we use the *mode weight factor* f_Region to quantify "regional" localization—this represents the relative contribution of each region of the system (base membrane

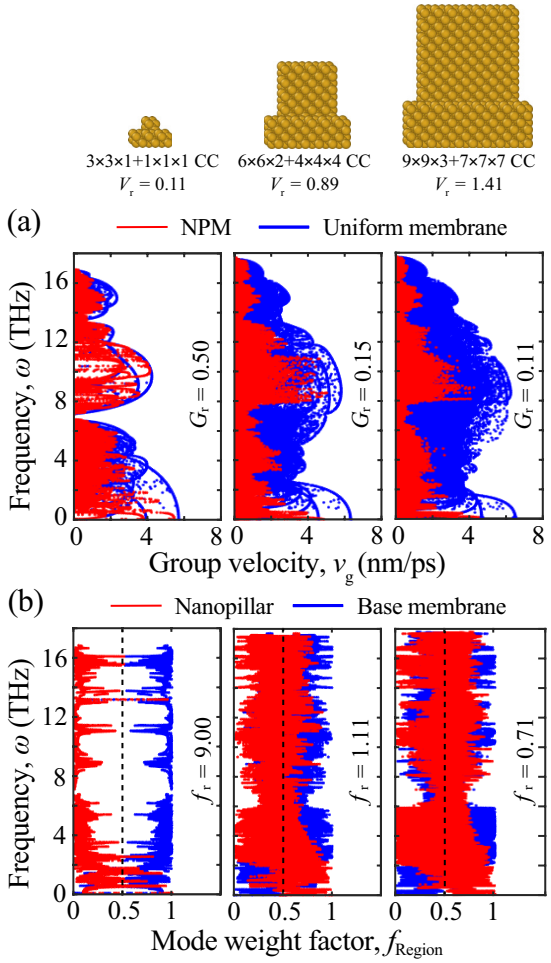

FIG. 5. Demonstration of the impact of the compensatory effect on the frequency distributions of (a) the group velocity and (b) the mode weight factor. These results are for the same three NPM configurations considered in Fig. 4b where the V_r value grows as the overall unit-cell size increases. Increasing V_r significantly decreases the group velocities and increases the degree of mode localization, across the full spectrum. This outcome is consistent with the decrease in the nonconformity factor observed in Fig. 4b.

or nanopillar) to each mode. This quantity is defined for each mode $(\boldsymbol{\kappa}, m)$ by [30–32],

$$f_{\text{Region}}(\boldsymbol{\kappa}, m) = \sum_{i=1}^{N_{\text{Region}}} \sum_{j=1}^{3} \boldsymbol{\phi}_{ij}^{*}(\boldsymbol{\kappa}, m) \boldsymbol{\phi}_{ij}(\boldsymbol{\kappa}, m), \qquad (3)$$

where $\boldsymbol{\phi}_{ij}(\boldsymbol{\kappa}, m)$ is the normal eigenmode corresponding to atom i and direction j. The $()^*$ symbol denotes the complex conjugate operation. The first summation is over the number of atoms N_{Region} for a region in the system (for example, $N_{\text{Region}} = N_{\text{Memb}}$ represents the number of atoms in the base membrane and $N_{\text{Region}} = N_{\text{Pillar}}$ represents the number of atoms in the nanopillar). The factor f_{Region} varies between 0 and 1. If the region of interest encompasses the total number of atoms in the system, i.e., $N_{\text{Region}} = N_{\text{Memb}} + N_{\text{Pillar}} = N$, the factor f_{Region} is equal to one. In order to quantify the relative contribution of each component of the unit cell, a mode weight factor ratio, f_{r}, is defined as $f_{\text{r}} = F_{\text{Memb}}/F_{\text{Pillar}}$, where F_{Region} represents the average value of f_{Region} over all the modes in the system and is computed in a similar manner to computing the average group velocity G. Following this definition, $F_{\text{Memb}} + F_{\text{Pillar}} = 1$. The ratio f_{r} varies between 0 (all the motion is localized within the nanopillar) and ∞ (all the motion is localized within the base membrane). The lower the f_{r} value, the higher the relative motion of the atoms in the nanopillar compared to the base membrane and therefore the higher the degree of mode localization in the nanoresonator. Figure 5b shows that higher V_{r} values yield lower f_{r} values, which is again consistent with the compensatory effect.

In summary, with vibrons compensation we observe a perfect correlation between the increase in phonon-vibron conformity on the one hand (which is represented by a decrease in $\hat{R}_{\text{pv}}$), and the reductions in G_{r} and f_{r} on the other hand. The consequence is a sustained increase in thermal conductivity reduction, compared to a uniform membrane, with increasing membrane thickness (see Section IV).

B. Frequency limits for "active" resonance hybridization

Thermal transport in silicon is carried by very short-wavelength waves and therefore there are lower frequency limits on the nanopillar generated vibrons that couple with the phonons. In bulk silicon, the transport is carried by phonons with wavelengths ranging, roughly, from 0.4 nm to 10 nm at room temperature with the majority of the distribution being within 0.4 nm to 2.2 nm [33]. In Fig. 6, we show the phonon dispersion curves for a uniform membrane unit cell of size $1 \times 1 \times 6$ CC (i.e., 0.5431-nm wide) and an NPM unit cell of size $6 \times 6 \times 6 + 4 \times 4 \times 12$ CC (i.e., 3.2586-nm wide). In principle, the Brillouin zone of this NPM unit cell may be unfolded six times and mapped on that of the uniform-membrane to enable direct comparison. In the figure, we consider the wavelengths of $\lambda = 0.54$, 1.09 and 10.86 nm and mark the frequency where each of these wavelengths intersects the lowest dispersion curve of the uniform membrane. The intercepts correspond to frequencies $\omega = 3.1$, 2.8 and 0.1 THz, respectively. These values represent the lower limits on the frequencies of vibrons that are capable of coupling with phonons at each of these wavelengths and lower. For example, any local resonance that is 2.8 THz or higher is, in principle, available for coupling with phonons with a wavelength of 1.09 nm or lower. Furthermore, we observe from Fig. 6a that the longitudinal acoustic branch extends to nearly 7 THz upon unfolding once. Thus the numerous vibrons spanning the 3-7 THz range are available for coupling and hybridization with a wide selection of phonons with wavelengths between 0.5 and 1 nm, and many more vibrons are active when also considering phonons with wavelengths larger than 1 nm. Upon examining closely the NPM dispersion curves (see inset of Fig. 6b), we observe that the vibrons for this example NPM structure start at 0.04 THz and populate as we move upwards; thus there are plenty of vibrons available for resonance hybridizations to take place within the full range of phonon wavelengths.

The only limiting factor that remains is the distribution of the phonon mean free path (MFP). For bulk silicon, the MFP distribution at room temperature ranges from a few nanometers to a few microns [33]. And for silicon membranes with a thickness on the order of a few tens or hundreds of nanometers, the room-temperature MFP distribution was shown in recent experimental results to comfortably cover a range that is at least on the order of the membrane thickness; see, for example, Refs. [14,34]. The active wavelengths (which as discussed above can be as small as a few angstroms) are able to travel relatively long distances within the pillared membrane structure as long as these distances fall within the range of the MFP distribution. An important advantage of molecular dynamics simulations is that all anharmonic and boundary scattering activity is accounted for and thus any limitations on the dynamical processes involving the nanostructure phonon and vibron modes are inherently incorporated in the results. The reader is referred to Ref. [16] where direct evidence of the existence of the resonance hybridization phenomenon in a room-temperature MD simulation was demonstrated using spectral energy density (SED) calculations [35 and 36]. In the next section, we use a different version of the SED method to further confirm the existence of localized modes and to examine the effect of resonance hybridizations on the phonon lifetimes and MFPs.

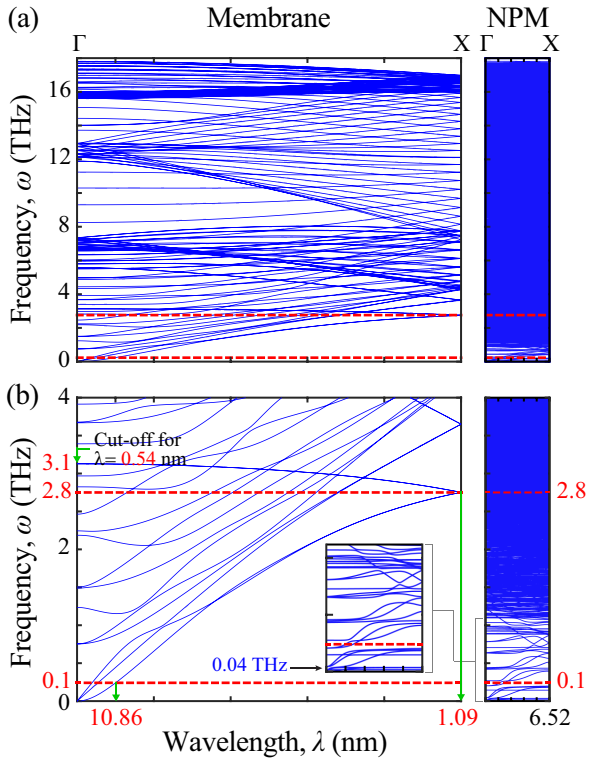

FIG. 6. Phonon band structure of a $6\times6\times6+4\times4\times12$ CC NPM unit cell (right) and a corresponding unpillared membrane modelled as a $1\times1\times6$ CC unit cell (left). Frequency-wavenumber intercepts are marked to illustrate the lower frequency limits for "active" vibrons considering phonons with wavelengths ranging from 0.54 nm to 10.86 nm. The full spectrum is shown in (a) and the $0\leq\omega\leq4$ THz portion is shown in (b).

III. EFFECT OF RESONANCES ON PHONON LIFETIMES AND MEAN FREE PATHS

In this section, we briefly investigate the effect of local resonances on the scattering properties of an NPM, namely the phonon lifetimes τ and MFPs $\Lambda=v_g\tau$. We use the SED method [35 and 36] to extract these quantities after running equilibrium molecular dynamics (EMD) simulations (EMD implementation details are in Appendix A). This technique predicts the phonon SED field Φ (or Φ'; see discussion below) at wave vector $\boldsymbol{\kappa}$ and frequencies ω by taking a superposition of $3N$ (total number of modes in the unit cell) Lorentzian functions

$$\Phi(\boldsymbol{\kappa},\omega)=\sum_{m}^{3N}\frac{I_0}{1+[2\tau(\omega_a-\omega))]^2}, \tag{4}$$

where I_0 is the SED peak, ω_a represents the anharmonic frequency of mode $(\boldsymbol{\kappa},m)$, and τ also corresponds to mode $(\boldsymbol{\kappa},m)$. In the literature, there are two formulations for computing SED: Φ and Φ'. Both methods are in principle the same although in practice they tend to produce slightly different results [37]. The former uses the normal mode velocity of the atoms and thus requires *a priori* knowledge of the phonon modes. The projection of atomic velocities onto the phonon modes is computationally demanding especially for large supercells such as NPM unit cells. However, the peaks are easily distinguishable in the Φ formulation and this allows us to predict the frequencies/lifetimes mode by mode. The Φ' formulation, on the other hand, requires only the atomic velocities and no modal projections are involved. This makes the predictions of the lifetimes in particular more challenging especially when the modes are closely spaced where identifying the peaks becomes difficult. However, the Φ' approach has the advantage that it requires less intensive computations. Here, we choose to use the Φ formulation which entails predicting all phonon information mode by mode. According to [36], Φ is computed by

$$\Phi\left(\boldsymbol{\kappa},\omega\right)=\mu_0\sum_{m}^{3N}\left|\int_0^{t_{\rm tot}}\dot{q}\left(\boldsymbol{\kappa},m;t\right)e^{-{\rm i}wt}{\rm d}t\right|^2, \tag{5}$$

where $\mu_0=\bar{m}/(2\pi t_{\rm tot}N_c)$, $\bar{m}$ is the mass of a silicon atom, $t_{\rm tot}$ is the total simulation time, and $\dot{q}$ is normal mode velocity,

$$\dot{q}\left(\boldsymbol{\kappa},m;t\right)=\sum_{j,i,l}^{3,N,N_c}\dot{u}_j\left(l,i;t\right)\phi^*_{ij}(\boldsymbol{\kappa},m)e^{{\rm i}\boldsymbol{\kappa}.\boldsymbol{r}_0(l,0)}, \tag{6}$$

where $\boldsymbol{r}_0$ is the equilibrium position vector of the lth unit cell, and $\dot{u}_j$ is the j-component of the velocity of the ith atom in the lth unit cell at time t. There is a total of $N_c=N_{c,x}N_{c,y}$ unit cells in the simulated computational domain. To predict the phonon anharmonic frequencies and lifetimes from Eqs. (4) and (5), each peak is fitted to a Lorentzian function centered at ω_a with a half-width at half-maximum value of $1/(2\tau)$.

We choose to study an NPM unit cell with the dimensions $3\times3\times3+1\times1\times3$ CC (240 atoms) and the corresponding uniform membrane unit cell with the dimensions of $3\times3\times3$ CC (216 atoms). The quasiharmonic LD dispersion diagrams for these single unit cells are shown as solid lines in Fig. 7a. As explained earlier, the velocity trajectories of atoms from EMD simulations and mode shapes from separately performed LD calculations are the main input for Eq. (5). Five independent simulations are performed under NVE conditions (constant number of atoms, volume, and energy) and are run for 2^{22} time steps using a 0.8-fs time step – the total simulation time is $t_{\rm tot}=3.4$ ns. The trajectories are output every 2^5 steps resulting in 2^{17} time steps. Several unit cells must be considered in the direction of interest (Γ-X in our case) to accurately predict frequencies at the allowed wave vectors and also ensure that there are no computational size effects due to periodic boundary conditions. We have considered two long simulation domains, consisting of $N_{c,x}=32$, and $N_{c,y}=1$ and $N_{c,y}=2$ single unit cells, respectively; the first consisting of 7,680 atoms and the second of 15,360 atoms. This results in 17 allowed wave vector points in the Γ-X path of the irreducible Brillouin zone. Using the EMD data and the

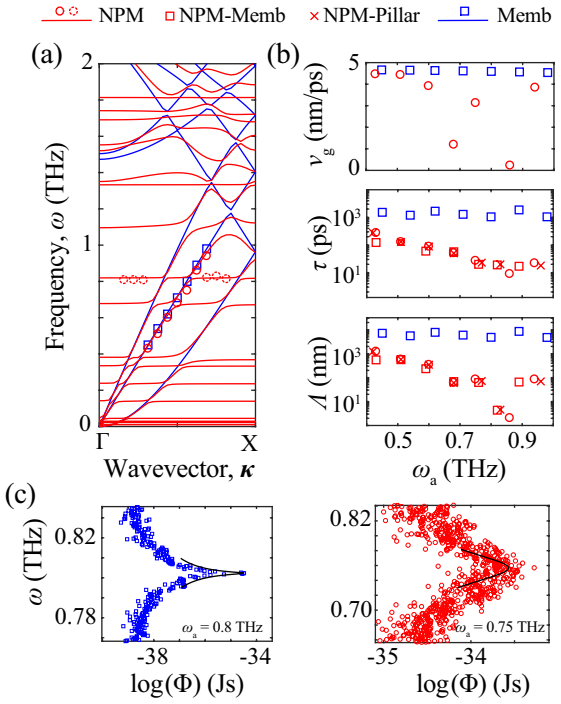

FIG. 7. (a) The quasiharmonic LD dispersion curves for the $3\times3\times3$-CC membrane unit cell and $3\times3\times3+1\times1\times3$-CC NPM unit cell are shown with the blue and red lines. The blue squares and red circles show the anharmonic frequencies extracted from EMD. (b) The group velocity, lifetime, and mean free path of the phonons marked in (a). The squares and crosses correspond to the NPM system when performing the SED calculations on the atoms only in the membrane or nanopillar portion, respectively. (c) SED peaks for the uniform membrane (left) and the NPM (right). The peak broadening in the NPM case is a manifestation of the effect of resonances. The black lines show the Lorentzian fits.

Φ formula, we have computed the frequencies and lifetimes of several transverse-acoustic (TA) phonon modes roughly in the range between 0.4-1 THz. The results are obtained based on peaks averaged over five simulations before curve fitting. Both simulation domains yield close results, which confirms that there is no significant computational size effect.

The anharmonic frequencies (squares and circles) for the calculated TA phonons are shown in Fig. 7a. Clearly, they closely match with the quasiharmonic dispersion curves (higher frequency phonons are expected to deviate from the quasiharmonic dispersion curves). The subset of data points falling along one of the horizontal lines (just below 1 THz) is direct evidence of the presence of localized modes. For frequencies lying along the phonon dispersion branch for shear-like waves, the lifetimes and MFPs are predicted and shown in Fig. 7b. The predictions for this low-frequency range reveal that the lifetimes and MFPs in an NPM are generally lower than in the corresponding uniform membrane, with a substantial decrease within the hybridization zones (for example, around 0.76 THz). It is evident, however, that these decreases in the the lifetimes and MFPs while significant, they are not too extreme because we are still able to identify and extract anharmonic frequencies (as shown in Fig. 7a) which is indicative of the presence of wave phenomena. The lifetimes and MFPs are also predicted for the membrane and nanopillar portions of the NPM system by respectively considering atoms in only the membrane or the nanopillar in the SED calculations. The results are close to the predictions made for the entire NPM system. The quasiharmonic group velocities of the same modes are also shown Fig. 7b for comparison. In Fig. 7c, we carefully examine an energy peak for each of the uniform membrane and the NPM. The left subfigure shows a frequency peak extracted from the SED data of the uniform membrane, which shows a sharp and distinguishable peak. In contrast, for the NPM mode shown in the right subfigure, the peak is broadened and thus the lifetimes are reduced. The reductions in the lifetimes/MFPs, as expected, are at and around the hybridization regions in the phonon band structure. Decreases in these quantities augment the reductions in the group velocities as well as the presence of mode localizations in causing an overall reduction in the thermal conductivity (compared to a corresponding uniform membrane).

In summary, it is of particular importance that the added anharmonic scattering stemming from the erection of the nanopillars on a membrane do not prevent the resonance hybridizations phenomenon from unfolding in a silicon NPM at room temperature. This observation is noted not only in the discrete anharmonic data in Fig. 7a, but also in Ref. [16] where a similar silicon-based NPM configuration was analyzed using SED (following the Φ' formulation) and the dispersion curves that emerged demonstrated clear evidence of ample resonance hybridization features. The extent to which each of the three mechanism−group velocity reductions, mode localization in the nanopillars, and decreases in the lifetimes/MFPs at and around the hybridization zones−relatively contribute to the overall thermal conductivity reduction will be investigated in future studies.

IV. NPM PERFORMANCE: EXTREME THERMAL CONDUCTIVITY REDUCTION

The size and geometry of the nanopillars are key to increasing the intensity of the resonance hybridizations effect, as demonstrated in Figs. 3 and 4. In this section, we extend our investigation to the prediction of the thermal conductivity and seek to further investigate the conditions for its extreme reduction. EMD simulations and the Green-Kubo (GK) method are used for the thermal conductivity calculations; see Appendix A for the implementation details. Lattice dynamics calculations together with the Boltzmann transport equation following the single-mode relaxation time approximation, and nonequilibrium molecular dynamics simulations, are also utilized for additional analyses provided in the appendices and these prediction methods too are

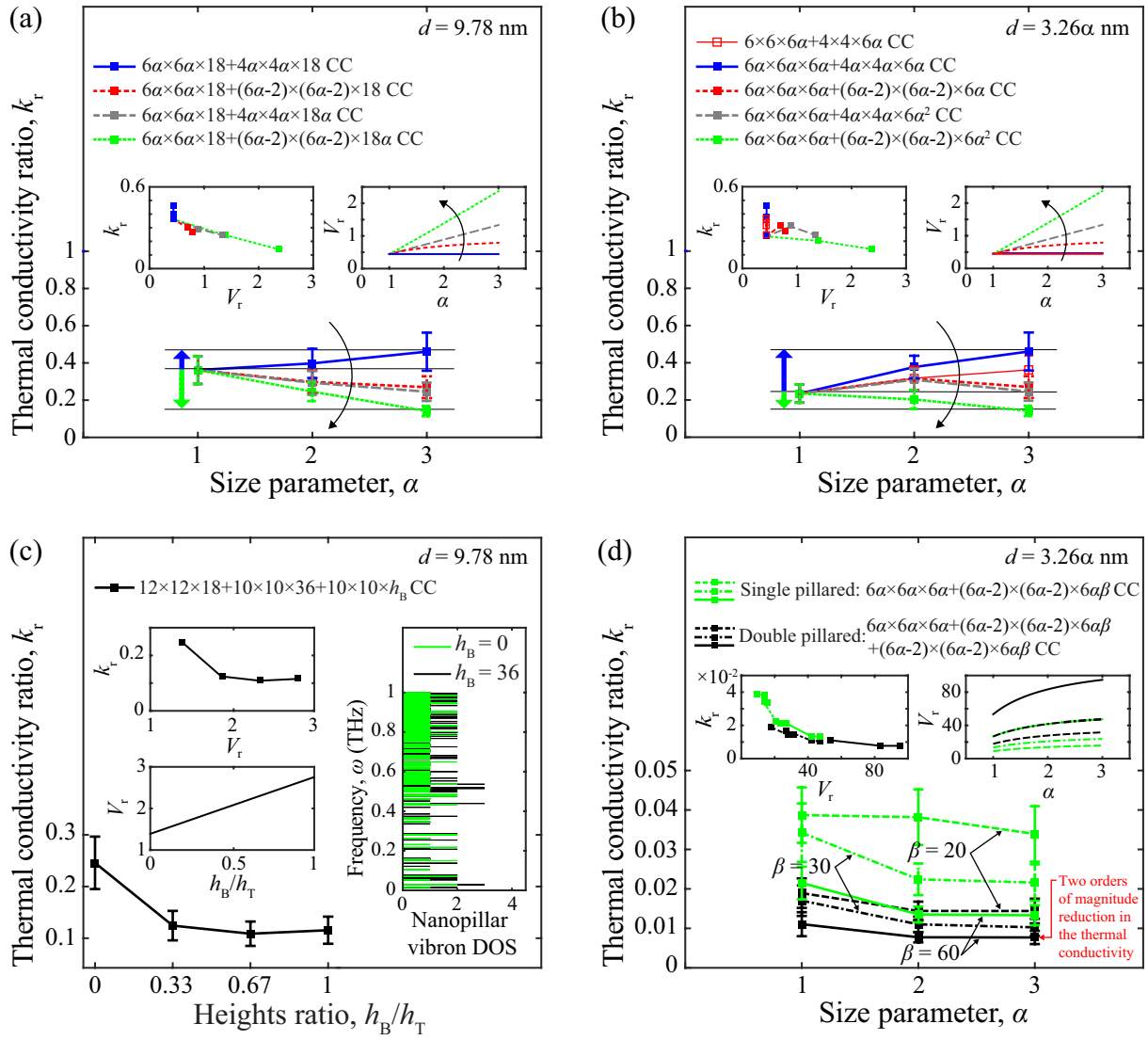

FIG. 8. Thermal conductivity ratio k_r versus the size parameter (scaling factor) α in (a), (b) and (d) and versus the ratio of top and bottom nanopillar heights h_T/h_B in (c). A membrane thickness of 6, 12, and 18 CC correspond to 3.26, 6.52, and 9.78 nm, respectively. Thick arrows in (a) and (b) represent maximum upward and downward changes among the cases considered. In each of (a), (b) and (d), the left inset shows k_r versus the nanopillar-to-base membrane volumetric ratio V_r (error bars not shown for brevity), and the right inset plots V_r versus α. In (c), the top left inset shows k_r versus V_r as h_T/h_B increases, the bottom left inset plots V_r as a function of h_T/h_B, and the right inset shows the vibrons DOS of a single- versus double-pillared NPM unit cell. Unlike in Fig. 3, here the vibrons DOS are extracted from the NPM band structure. In (d), β denotes the nanopillar height divided by the membrane thickness. All trends clearly show that the performance of an NPM in reducing k_r is directly dependent on V_r and the type of α-dependency. In the double-pillared configuration considered in (d), a two orders of magnitude reduction in the thermal conductivity is recorded.

described in Appendix A.

A. NPM size, geometric, and temperature effects on thermal conductivity reduction

In Fig. 8, we investigate using the EMD-GK scheme the reduction in the in-plane thermal conductivity for various NPM sizes and geometries. The reduction is represented by k_r, the lattice thermal conductivity of a membrane with nanopillar(s) in the unit cell divided by that of a uniform membrane with the same thickness. Key factors in this analysis are (i) V_r and (ii) the manner by which the geometry of the different NPM components (membrane and nanopillar) change relative to each other as the size is increased. Using α as a size parameter, we refer to the latter factor as the "α-dependency". The mathematical representation of the various α-dependencies considered, their corresponding V_r values, and other related quantities are given in Table B.1 in Appendix B. A corresponding graphical repre-

sentation is provided in the insets of Fig. 8 in the form of V_r vs. α, V_r vs. h_T/h_B, and k_r vs. V_r.

The results in Figs. 8a and 8b show that regardless of the specific form of the α-dependency, k_r increases with size when V_r is constant. We have shown in an earlier study that this behavior correlates with the degree by which the resonance hybridizations affect the group velocities as a unit cell is proportionally upscaled in size [17]. For k_r to maintain its value with α, or possibly even drop in value, we need to introduce compensation (as discussed in the previous sections) to the α-dependency; that is, to select the dependency in a manner such that V_r increases as α increases. The strength of this compensation is measured by $\gamma = dV_r/d\alpha$. We observe that indeed k_r drops, as desired, for the cases exhibiting a compensatory α-dependency, e.g., k_r drops from 0.36 at $\alpha = 1$ to 0.14 at $\alpha = 3$ for the $6\alpha \times 6\alpha \times 18 + (6\alpha - 2) \times (6\alpha - 2) \times 18\alpha$ CC model for which $V_r = \alpha(1 - 1/3\alpha)^2$ and $\gamma = (1 - 1/9\alpha^2)$. This negative trend in thermal conductivity reduction is attributed to what we described earlier as the *compensatory effect*. The connection between k_r and the α-dependency, with and without compensation, correlates directly to the reduction in the group velocities and the increase in mode localizations that arise due to the resonance hybridizations. A demonstrative case study on these correlations is provided in Appendix B.

In Fig. 8c, we examine the influence of adding a second nanopillar (at the bottom) of the membrane. The right inset demonstrates that this significantly increases the spread in the vibrons DOS spectrum, and as a result k_r drops from 0.25 to 0.12.

In Fig. 8d, we examine different nanopillar heights by varying the parameter β.[38] It is shown that the larger the value of β [i.e., the taller the nanopillar(s)], the stronger the reduction in k_r—which allows us to attribute additional incremental reductions in k_r with increases in nanopillar height to the wave-resonance coupling phenomenon rather than boundary scattering. This is consistent with observations in previous studies of NPMs [16,23,39]. Pushing the compensatory effect further, we show in Fig. 8d a reduction in the thermal conductivity by a factor of 75 for a single nanopillar and a factor of 130 for double nanopillars for a membrane 9.78-nm thick with each nanopillar extending up to 586.5 nm in height. The extent of these reductions is unprecedented in the literature, and yet more reductions are possible with further increases in nanopillar size and augmentation with conventional treatments such as optimized alloying [39].[40]

Additional investigations of NPM design avenues are summarized in Appendices C, D, and E. For example, in Appendix E, the nanopillars are replaced by nanowalls which are shown to provide yet further reduction in the thermal conductivity.

Lastly, we examine the effect of temperature on the performance of the best performing design considered in Fig. 8d, namely the double-pillared membrane with α=3 and β=60. At a temperature of 700 K, we obtain a value of $k_r = 0.0519 \pm 0.0085$ which corresponds to nearly a factor of 19 reduction in the thermal conductivity compared to a uniform membrane withe same thickness of 9.78 nm.

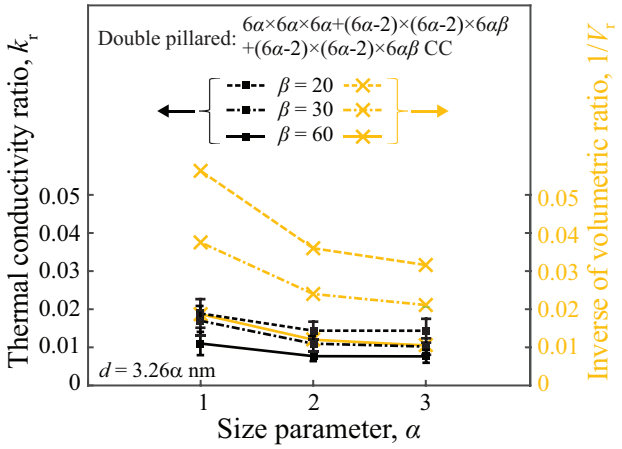

FIG. 9. Demonstration of the positive correlation between the thermal conductivity reduction and the inverse of the nanopillar-to-membrane volumetric ratio. This correlation provides a simple geometric metric that may be used to obtain a rough prediction of the trends of k_r versus α for different NPM unit-cell configurations.

B. Correlation of NPM analytical geometric trends with k_r predictions from MD simulations

As explained in Section I and demonstrated in Section II and Appendix B, the resonance hybridization phenomenon (1) causes the group velocities of many of the base membrane phonon modes to reduce significantly, and (2) adds numerous zero-group velocity modes (vibrons) to the system. It is shown in Section III that resonance hybridizations also reduce the phonon lifetimes at and around the coupling regions with the phonon band structure. Each of these three factors contribute to the reduction of k_r. Since the intensity of these effects depend on the number of vibrons added to the system, we may predict the extent of the thermal conductivity reduction indirectly from V_r (especially that we also saw, from Fig. 4, that a rise in V_r causes an increase in the phonon-vibron conformity, i.e., a drop in $\hat{R}_{pv}$). This correlation is demonstrated in Fig. 9 which plots both k_r and $1/V_r$ versus the size parameter α for the three different double-pillar configurations considered in Fig. 8d.

It is observed that both trends decrease with increase in α due to the compensatory effect. It is also observed that this decrease takes place with a decreasing rate, which is for the two following reasons. First, as more vibrons are added, the effect of additional vibrons gradually diminishes as the dispersion curves get saturated with resonance hybridizations. This factor is evident in both the k_r and $1/V_r$ trends. Second, as the NPM characteristic size increases, this size compared to the MFP dis-

tribution increases, which in turn leads to a diminishing of the effects of resonance hybridizations. The latter factor pertains to only the k_r trends, and we indeed observe a slightly less negative slope for the k_r curves compared to the $1/V_r$ curves. As discussed earlier, the MFPs factor for an NPM made of silicon will become practically influential in hindering wave and resonance phenomena at significantly higher NPM dimensions than the dimensions considered in this investigation. This factor becomes less influential as the temperature is reduced.

V. CONCLUSIONS

In Ref. [15], a new type of nanostructured material was introduced that enables a reduction in the lattice thermal conductivity through the phenomenon of full-spectrum resonance hybridizations. Unlike materials that naturally exhibit local resonances from rattling atoms, such as clathrates [41], an NPM includes artificially introduced local nanoresonators as substructures that may be attached to the host material (for example, nanopillars standing on a silicon membrane). With this concept, and given that we can size the nanoresonators as desired, we yield a tremendous number of hybridizing resonances that may be engineered to span roughly the entire spectrum of the host material. If the relevant unit-cell dimensions fall within the range of the phonon MFP distribution, each of these resonances will (1) cause a reduction in the group velocities of existing heat carrying modes (phonons), and (2) introduce localized modes (vibrons) that absorb but not transfer heat−these two effects work in tandem and could be tuned to attain a significant reduction in the transport medium's thermal conductivity. Drops in the phonon lifetimes also take place−at and around the hybdrization zones in the phonon band structure−leading to further reduction in the thermal conductivity. Direct evidence of the existence of resonance hybridizations in nanopillared silicon membranes at room temperature was provided in a subsequent study using spectral energy density analysis of atomic motion from MD simulations [16]. Therefore the reductions in the lifetimes, while relatively significant in the coupling regions, are still moderate enough overall not to impede the occurrence of the phonon-vibron couplings which are of coherent nature.

More recently, it was discovered that the performance of an NPM deteriorates as the unit-cell size is increased [17]. This property is detrimental because it impedes the feasibility of upscaling to sizes that are suitable for thermoelectric device integration, which is needed to enable industrial-scale deployment for waste heat conversion to electricity and for cooling and refrigeration. Furthermore, parameter optimization studies have shown that the inclusion of nanoresonators could reduce the thermal conductivity by at most a factor of five [17,23,39]. In this paper, we reveal a route that reverses the unfavorable size-effect trend and causes the thermal conductivity reduction to increase, rather than decrease, with size. The key is the notion of vibrons compensation, that is, to enlarge the nanoresonator at a higher rate than the base membrane as larger unit-cell sizes are considered. In addition to enriching the band structure with a higher vibron-to-phonon ratio, this approach causes an increase, rather than a decrease, in the conformity between the phonon and vibron DOS distributions. The outcome is not only favorable for upscaling, but it is also extremely advantageous in that it allows the unit-cell design space to expand thus opening up a path for a significant increase in the effectiveness of the resonance hybridizations phenomenon, as quantitatively demonstrated in Fig. 4. Effective resonance hybridizations lead to not only a magnification in the intensity of phonon group-velocity reductions, but also a boost in mode localizations (as explicitly demonstrated in Fig. 5 and Appendix B), and a noticeable decrease in a substantial fraction of the population of phonon lifetimes (as shown in Fig. 7). This in turn grants us a route for unprecedented reductions in the thermal conductivity.

From our calculations, the thermal conductivity of a 9.78-nm thick uniform silicon membrane is 3.7 ± 0.7 times lower than the bulk form. Multiplying this by the factor of 130 ± 28 for the best double-nanopillar case reported in Fig. 8d gives a total factor of 481 ± 55, which corresponds to roughly half the thermal conductivity of bulk amorphous silicon (see Appendix F). By conservatively assuming the same k_r value for $\alpha = 6$ for this high performing configuration, a 19.55-nm thick NPM would exhibit a thermal conductivity reduction by a factor of 311 ± 85 with respect to bulk silicon.[42] Assuming a one-to-one mapping between the thermal conductivity reduction and the increase in ZT−as demonstrated by the experimental characterization of similarly sized freestanding silicon membranes [11] and silicon nanowires [13],[43] and given that the ZT of moderately doped bulk silicon at $T = 300$ K is 0.01 [44,45], we obtain a projected room-temperature ZT value of 3.1 ± 0.9.[46] This is significantly higher than any previously reported ZT value at any temperature, [47] not only for silicon but for thermoelectric materials in general.

ACKNOWLEDGMENTS

This research was partially supported by the National Science Foundation (NSF) CAREER Grant No. 1254931 and the Smead Faculty Fellowship program. The authors thank current group member Mr. Dimitri Krattiger and GULP developer Dr. J. D. Gale for their insights on the LD calculations, and former group member Dr. Lina Yang for setting up and conducting the NEMD simulations presented in Appendix A. This work utilized the Janus supercomputer, which is supported by NSF Grant

No. CNS-0821794 and the University of Colorado Boulder. This work also used the Extreme Science and Engineering Discovery Environment (XSEDE) Bridges resource at the Pittsburgh Supercomputing Center through allocation DMR160036P, which is supported by National Science Foundation grant number ACI-1548562 [48].

Appendix A: Thermal conductivity prediction methods

Equilibrium molecular dynamics simulations

Thermal conductivity predictions in this investigation are obtained primarily using equilibrium molecular dynamics simulations and the Green-Kubo method [49,50,51,52]. In the GK method, the lattice thermal conductivity tensor $\boldsymbol{k_l}$ is calculated from the heat current auto-correlation function (HCACF) by

$$\boldsymbol{k_l} = \frac{1}{k_B V T^2} \int \langle \boldsymbol{J}(0) \otimes \boldsymbol{J}(t) \rangle dt, \tag{A1}$$

where k_B is the Boltzmann constant, V is the total volume of the system including both membrane and nanopillar portions (i.e., volume of the unit cell $aA_x \times aA_y \times d + b\times b\times h_T + b\times b\times h_B$ in a simulation domain consisting of a single unit cell), $\boldsymbol{J}$ is the heat current vector (in the units of energy times length per unit time) computed over all atoms in the system, and $\otimes$ denotes the tensor product operation. As defined earlier, T is the temperature and t is the time. The integrand $\langle \boldsymbol{J}(0) \otimes \boldsymbol{J}(t) \rangle$ represents the time average of the HCACF.

Throughout the investigation, we recall that the crystals are assumed to be defect-free and interatomic interactions are modeled using the Stillinger-Weber empirical potential [26]. All simulations are performed using the LAMMPS software and the heat current vector is evaluated using the stress-based formula

$$\boldsymbol{J} = -\sum_i \boldsymbol{S}_i \boldsymbol{v}_i, \tag{A2}$$

where $\boldsymbol{S}_i$ and $\boldsymbol{v}_i$, respectively, denote the virial stress tensor and the velocity vector for atom i [53]. The computational domain for the NPM models and the uniform membrane models consists in each case of one unit cell with standard periodic boundary conditions applied at the in-plane boundaries leaving the surfaces free in the z-direction [16, 17]; see Fig. 1 for an illustration of the unit-cell geometries considered and the associated notation. The computational domain for the bulk case consists of a cubic unit cell with periodic boundary conditions applied in all three directions.

The systems are initially equilibrated for 1 ns, with a time step $\Delta t = 0.8$ fs, at room temperature ($T = 300$ K) under the NPT ensemble (zero pressure cell size based on constant number of atoms, pressure, and temperature). The simulations are subsequently allowed to run under the NVE ensemble for an additional 6 ns to collect heat fluxes that are recorded every 4 fs. The 6-ns time span is sufficiently long compared to the longest phonon lifetime to reliably predict the thermal conductivity. With these parameters, the HCACFs generally converge within the first 1 ns, with the rate of convergence depending on the type of the material system [e.g., bulk, uniform membrane, or NPM]. The smaller the value of the predicted thermal conductivity, the shorter the convergence time. The x-direction HCACF (normalized with respect to its initial value) for the NPM system with the best performance (double pillared with $\alpha = 3$ and $\beta = 60$) is shown in Fig. A.1a. The normalized HCACFs of a corresponding uniform membrane (i.e., a silicon membrane with the same thickness but without nanopillars) and the bulk case are also shown. The x-direction thermal conductivity (denoted k_l) for the NPM system, which is observed to have converged within the 100 to 200 ps window, is plotted in Fig. A.1b; and in the inset, the thermal conductivities of the uniform-membrane and bulk cases are shown as well. To minimize modeling errors, the quantity reported is k_r which as defined earlier is the NPM lattice thermal conductivity divided

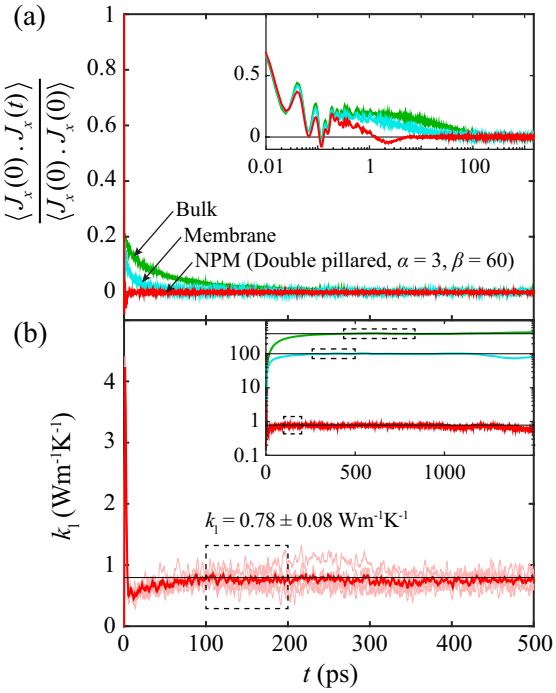

FIG. A.1. EMD-GK: (a) Normalized HCACF for the double-pillared NPM system with size and pillar-to-membrane aspect ratio parameters of $\alpha = 3$ and $\beta = 60$, respectively. The uniform-membrane and bulk HCACFs are also shown in the background. The same curves are provided in the inset with the time axis plotted in logarithmic scale. (b) Calculated lattice thermal conductivity for the NPM system considered in (a). Twelve thermal conductivity predictions are shown in light red, and the average value is in dark red. The dashed box highlights the converged value of k_l. In the inset, the uniform-membrane and bulk thermal conductivities are also shown along with boxes indicating the convergence regions.

by that of a corresponding uniform membrane with the same thickness. For each prediction of k_r, an average value is obtained from six independent simulations with different initial velocities. Furthermore, both the x- and y- in-plane directions are considered for all NPM and uniform membrane calculations−effectively resulting in an averaging over twelve predicted values. For bulk silicon, the reported thermal conductivities are the average of values obtained by simulating three unit cells of different sizes, each simulated also six times, and, in addition, evaluations are made over the x-, y- and z-directions−effectively resulting in an averaging over fifty-four predicted values. The unit cells considered for the bulk simulations are $6 \times 6 \times 6$ CC, $12 \times 12 \times 12$ CC, and $18 \times 18 \times 18$ CC−the predicted thermal conductivity for each is 412±32, 319±28, and 397±36 $\mathrm{Wm^{-1}K^{-1}}$, respectively. Thus no discernible computational size effect is observed among these three unit-cell sizes, which is consistent with what others have observed in similar investigations [54, 55].

The thermal conductivities predicted using the EMD-GK method and the adopted empirical potential are overestimated in terms of absolute quantities; however, this method is able to reliably predict accurate physical trends [50, 54, 55]. In all the EMD simulations, the reported error bars are calculated using the standard error of the mean, S.

For uncertainty quantification of any multivariate function $Q(k_1 \pm S_{k_1}, k_2 \pm S_{k_2}, ...)$, where k_1, k_2, etc., represent the thermal conductivity of a specific system, and each of S_{k_1}, S_{k_2}, ... denotes the corresponding error−for example, considering Q as the ratio of NPM thermal conductivity with respect to that of the uniform membrane, $Q = (k_{\mathrm{NPM}} \pm S_{k_{\mathrm{NPM}}})/(k_{\mathrm{Memb}} \pm S_{k_{\mathrm{Memb}}})$−the following formula is used [56]:

$$S_Q = \sqrt{\sum_i \left(\frac{\partial Q}{\partial k_i} S_{k_i}\right)^2}. \tag{A3}$$

Using this simulation framework, the thermal conductivity of a uniform membrane is predicted and listed in Table A.1 for various thicknesses d. These values are identical to those reported in Ref. [17], and the prediction for bulk silicon is in good agreement with other predictions in the literature where the simulation setup is similar [54, 57].

Nonequilibrium molecular dynamics simulations

Another commonly used technique for lattice thermal conductivity predictions is based on nonequilibrium molecular dynamics (NEMD) simulations and direct application of Fourier's law of heat conduction [51, 54, 58]. While this route is not used in any of the analyses presented in the main sections or the other appendices, here we briefly review the technique and provide some results to enable a comparison with predictions based on the EMD-GK approach.

α	d (CC)	d (nm)	k_{l} ($\mathrm{Wm^{-1}K^{-1}}$)
1	6	3.26	47 ± 9
2	12	6.52	76 ± 11
3	18	9.78	101 ± 19
6	36	19.55	157 ± 27
Bulk	–	–	376 ± 19

TABLE A.1. Thermal conductivity of uniform silicon membranes and bulk silicon using EMD simulations and the GK method. The membrane unit-cell size is $6\alpha \times 6\alpha \times d$ CC, where α is a size parameter (scaling factor) and $d = 6\alpha$ is the thickness. Three unit-cell sizes are considered for the bulk case: $6 \times 6 \times 6$ CC, $12 \times 12 \times 12$ CC, and $18 \times 18 \times 18$ CC. The bulk thermal conductivity value is averaged over these three sizes.

For a system subjected to a spatial temperature gradient $\boldsymbol{\nabla} T$ across its boundaries, the Fourier's law of conduction states that the steady-state heat current density vector $\boldsymbol{j}$ (which is a microscopic vector of an effective heat current density defined as a quantity of energy per unit time per unit area) is

$$\boldsymbol{j} = -\boldsymbol{k_{\mathrm{l}}} \boldsymbol{\nabla} T. \tag{A4}$$

Equation (A4) is a general form of the law that defines volumetric heat current and is applicable even when the medium does not exhibit a uniform cross-sectional area. For an NPM, the quantity $\boldsymbol{j}$ is related to $\boldsymbol{J}$ [which is the total nonvolumetric effective heat current vector calculated using Eq. (A2)] by $\boldsymbol{j} = \boldsymbol{J}/V$, where V as stated earlier is the volume of the entire system−including both the base membrane portion and the nanopillar portion.

The technique applies to a finite, multiple unit-cell system. As an example, we consider the five unit-cell model of an NPM shown in Fig. A.2a and consider the x-component of $\boldsymbol{k_{\mathrm{l}}}$. A pair of Langevin heat baths is used to create a temperature gradient $\partial T/\partial x$, where $T = 1/(3N_x k_{\mathrm{B}}) \sum_{i=1}^{N_x} m_i \|\boldsymbol{v}_i\|^2$, $N_x = N_{x,\mathrm{base}}$ or $N_x = N_{x,\mathrm{base}} + N_{x,\mathrm{pillar}}$ is the number of atoms over the entire cross section at position x, and m_i and $\boldsymbol{v}_i$ denote, respectively, the mass and velocity vector of the ith atom (in our model m_i is constant and is equal to the mass of a silicon atom which, as defined earlier, is denoted by $\bar{m}$). The temperature definition shows that, at each position x, the kinetic energy of all the atoms should be considered (including the atoms in the nanopillar as they have nonzero velocity) to correctly obtain the correct temperature profile through the system. This is done by setting the temperature of the left and right ends at $T_L = 310$ K and $T_R = 290$ K, respectively. Periodic boundary conditions are applied in the y-direction and the surfaces are kept free along the z-direction. We simulate this nonequilibrium system for 0.8 ns to reach the steady state and then run it for another 9.6 ns to obtain the average heat flux and temperature profile.

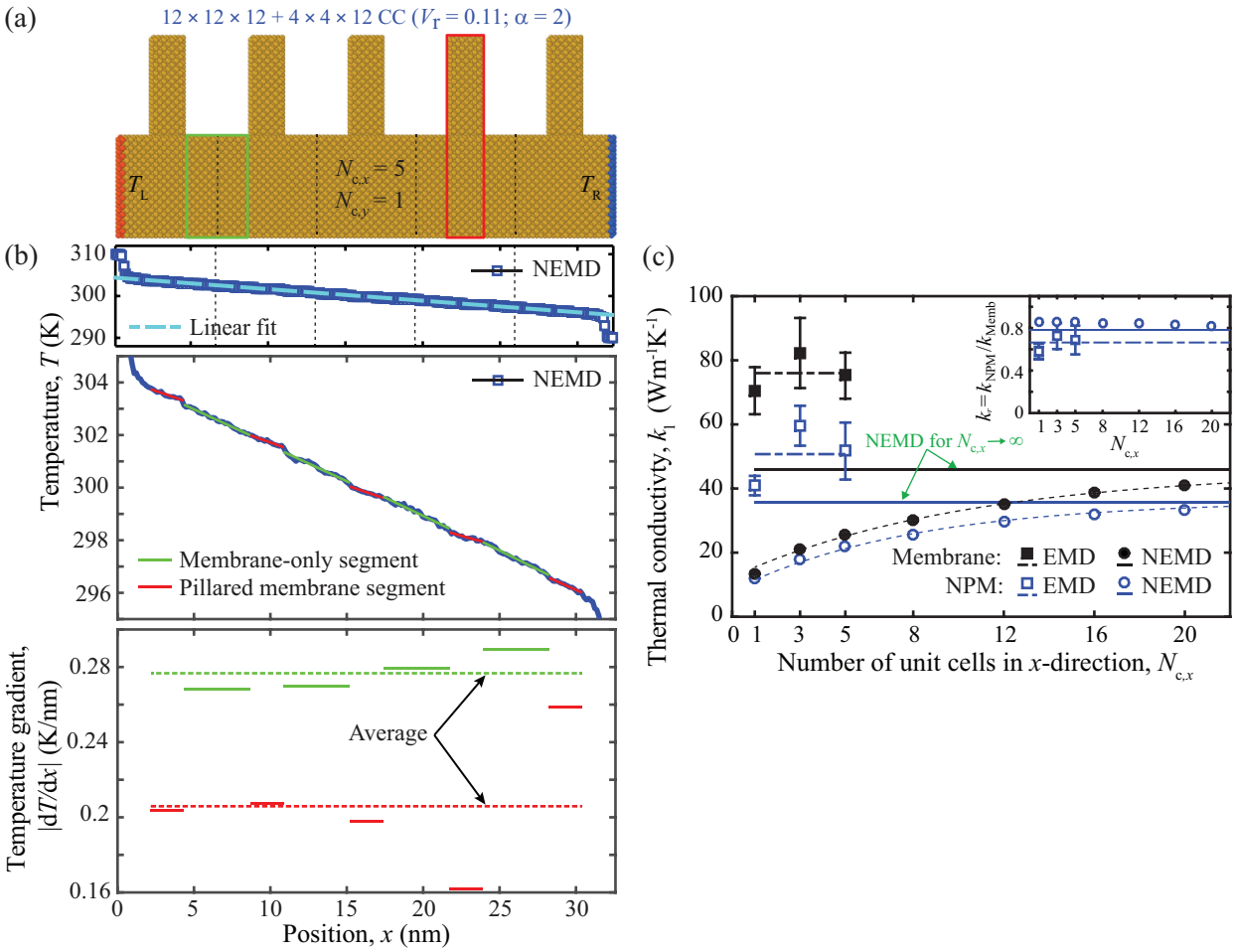

FIG. A.2. NEMD-Fourier: (a) Schematic of NEMD simulation setup consisting of $N_{c,x} = 5$ and $N_{c,y} = 1$ NPM unit cells along the x- and y-directions, respectively. (b) Temperature profile with linear fit (top), temperature profile in high resolution (middle), and temperature gradient (bottom) across the finite dimension. The piecewise variation in the temperature profile is due to the division of the system into membrane-only segments and pillared membrane segments. (c) Thermal conductivity as a function of number of unit cells along the direction of the temperature gradient (shown in normalized form in the inset). The curved dashed lines represent exponential fittings. The horizontal lines represent average values for the EMD-GK results (dashed) and converged values for the NEMD-Fourier results (solid). This figure is similar to Fig. 4 in Ref. [17] except here the total volume of the NPM unit cell is considered in the NEMD-Fourier k_l predictions, rather than the volume of the base membrane portion only.

As shown in Fig. A.2, the temperature profile emerging from simulations along the direction of periodicity is not smooth; this is because the value of the cross-sectional area changes in a piecewise mnanner as the heat is transported along the membrane, based on whether or not there is a nanopillar. Thus in using the Fourier law to calculate $\boldsymbol{k_l}$, Eq. (A4) is replaced with $\boldsymbol{j} = -\boldsymbol{k_l}\boldsymbol{\nabla} T_{\text{lin}}$, where $\boldsymbol{\nabla} T_{\text{lin}}$ represents a linear fit of the temperature gradient along the multiple unit-cell system. The reported thermal conductivity values are the average of two independent simulations.

Because the NEMD-Fourier technique is based on a finite system with fixed boundaries, a relatively large number of unit cells is usually required to adequately remove erroneous size effects [52,54]. In Fig. A.2b, k_l is predicted as a function of the totall number of unit cells in the x-direction $N_{c,x}$ (in a layout consisting of only one cell in the y-direction.). Estimates of the converged values of the thermal conductivity are obtained by performing an exponential extrapolation on the data points. By comparing these results with counterparts from the GK-EMD method, it is seen that the thermal conductivity values predicted by NEMD-Fourier are lower than the corresponding EMD-GK predictions. However, importantly, the predicted thermal conductivity reductions from the two methods agree well (see the inset of Fig. A.2b). The k_r values computed by EMD-GK are at most 15% smaller than the corresponding NEMD-Fourier predictions.[59]

Boltzmann transport equation

In some cases, whenever stated in the text, the lattice thermal conductivity is predicted using the Boltzmann transport equation (BTE) under the assumptions of the single-mode relaxation time (SMRT) approximation [60] and an isotropic Brillouin zone. In this method, k_l is evaluated by

$$k_{\rm l} = \underbrace{\frac{1}{V}\frac{A_{\rm c}}{4\pi}\sum_{m}\int_{0}^{\kappa_{\max}} C(\kappa,m)v_{\rm g}^2(\kappa,m)\tau(\kappa,m)\kappa d\kappa}_{K_{\rm l}}, \quad \text{(A5)}$$

where $A_{\rm c}$ is the unit-cell base area (i.e., area spanned by the region $aA_x \times aA_y$ of the unit cell), C denotes the specific heat, and V, $v_{\rm g}$, and τ are as before the total volume of the system (including the base membrane and nanopillar portions), the group velocity, and the scattering time constant (lifetime), respectively. The integration is over all phonon wavenumbers from $\kappa = 0$ to $\kappa_{\max} = \pi/(aA_x)$ [or $\pi/(aA_y)$] for branch number m and the summation is over all the phonon branches. The nonvolumetric lattice thermal conductivity is denoted K_l.

In Eq. (A5), the phonon specific heat C for each mode is computed according to the Bose-Einstein distribution,

$$C(\kappa,m) = k_{\rm B}\frac{\chi^2 e^{\chi}}{(e^{\chi}-1)^2}, \quad \text{(A6)}$$

where $\chi = \chi(\kappa,m) = \hbar\omega/k_{\rm B}T$ and $\hbar$ is the reduced Planck constant. In the classical limit as $T \to \infty$, Eq. (A6) approaches k_B. The phonon band structure and group velocities are obtained by performing quasi-harmonic lattice dynamics (LD) calculations [61]. For unit-cell models featuring a large number of degrees of freedom, these calculations are accelerated using the RBME technique [27]. In the present implementation of the RBME technique, a 3-point expansion is conducted whereby eigenvectors are selected at the Γ, Δ, and X points within the irreducible Brillouin zone to form reduced bases which are then used for the calculations at other wavenumbers. This procedure generates dispersion curves along the Γ-X path at more than an order of magnitude higher speed with errors less than 1% compared to the full (non-reduced) calculations. Finally, the scattering time constants are modeled following Matthiessen's rule

$$\tau^{-1}(\kappa,m) = \tau_{\rm U}^{-1} + \tau_{\rm I}^{-1} + \tau_{\rm B}^{-1}, \quad \text{(A7)}$$

where $\tau_{\rm U}$, $\tau_{\rm I}$, and $\tau_{\rm B}$ denote specific relaxation time constants associated with umklapp scattering, impurity scattering, and boundary scattering, respectively. For each of these quantities, we follow our earlier model in Ref. [15] where $\tau_{\rm U}^{-1} = AT\omega^2 e^{-B/T}$, $\tau_{\rm I}^{-1} = D\omega^4$ and $\tau_{\rm B}^{-1} = |v_{\rm g}|/l$. The length parameter is selected to represent non-specular surfaces, i.e., $l = d$. The material parameters A, B, and D are obtained from curve fits to experimental data on uniform silicon membranes as detailed in Ref. [15] and summarized in Table A.2 for membranes with a thickness of d = 6, 12 and 18 CC. These scattering parameters are used for both uniform and pillared membrane models.

Thickness, d (CC)	6	12	18	Bulk
A [$\times 10^{-19}$] (s/K)	4190.00	80.20	30.10	2.20
B (K)	705.62	373.90	299.15	178.15
D [$\times 10^{-45}$] (s^3)	1.32	1.32	1.32	1.32

TABLE A.2. Empirical relaxation time parameters used in the BTE-SMRT models

Definition of NPM volume V in thermal conductivity models

In all the three methods described above for thermal conductivity prediction, namely, the GK-EMD, NEMD-Fourier, and the BTE-SMRT methods, we have emphasized that the total volume V of the NPM system (or unit cell if the computational domain consists of only a single unit cell) consists of *both* the base membrane and the nanopillars portions. In all these formulations, the normalization by the total volume V is necessary to correctly express the volumetric heat capacity $c_{\rm sys}$ of the NPM nanostructure—which is a quantity influenced by the motion of all the atoms and the characteristics of all the modes in the system. This point is elucidated in the following short review of pertinent fundamental formulations from statistical thermodynamics.

In real space, which is relevant to the EMD-GK and NEMD-Fourier methods, the nonvolumetric heat capacity for a single DOF of atomic motion at a constant volume is defined as $C_q = \partial E_q/\partial T$, where E_q is the total energy (potential energy plus kinetic energy) of the qth DOF. Thus the volumetric heat capacity for a system with N atoms (each atom has 3 DOF) is calculated as $c_{\rm sys} = (1/V)(\partial E/\partial T)$, where $E = \sum_{q=1}^{3N} E_q$ is the total energy of the system [62].

Considering the mechanics of a quantum-harmonic oscillator, the energy of the qth DOF is defined as [63,64]

$$E_q = \hbar\omega_q[\frac{1}{2} + f_q^{(0)}], \quad \text{(A8)}$$

where ω_q is the oscillator frequency, $f_q^{(0)} = 1/(e^{\chi_q}-1)$ is the Bose-Einstein equilibrium distribution function, and $\chi_q = \hbar\omega_q/k_{\rm B}T$. Upon differentiation with respect to T, the nonvolumetric heat capacity of the qth DOF is

$$C_q = \hbar\omega_q\frac{\partial f_q^{(0)}}{\partial T}. \quad \text{(A9)}$$

It follows that the corresponding quantity per unit volume is

$$c_q = \frac{\hbar\omega_q}{V}\frac{\partial f_q^{(0)}}{\partial T}, \quad \text{(A10)}$$

and the volumetric heat capacity of the system is

$$c_{\text{sys}} = \frac{1}{V}\sum_{q=1}^{3N} \hbar\omega_q \frac{\partial f_q^{(0)}}{\partial T}. \tag{A11}$$

The motion of all the atoms in the system, including the base membrane and nanopillar portions, necessarily contribute to the definition of c_{sys} because both portions form a contiguous integrated internal structure.

By taking the classical limit of $f_q^{(0)}$ as $T \to \infty$, Eq. (A11) is simplified to

$$c_{\text{sys}} = \frac{3Nk_{\text{B}}}{V}. \tag{A12}$$

Although Eq. (A12) describes a classical-harmonic heat capacity while the heat capacity in MD simulations is inherently a classical-anharmonic quantity, it is a reasonable assumption to approximate the heat capacity of each DOF by k_{B} when predicting properties of silicon (for both bulk and nanostructures) at room temperature [65,66].

In phonon space, which is relevant to the BTE-SMRT method, the energy of each mode is similarly defined as [67]

$$E(\boldsymbol{\kappa}, m) = \hbar\omega(\boldsymbol{\kappa}, m)[\frac{1}{2} + f^{(0)}(\boldsymbol{\kappa}, m)]. \tag{A13}$$

Here, for simplicity, we drop the index and identify each mode by a particular wave vector $\boldsymbol{\kappa}$ and branch number m. From Eq. (A13), the nonvolumetric heat capacity of a mode is

$$C(\boldsymbol{\kappa}, m) = \hbar\omega(\boldsymbol{\kappa}, m)\frac{\partial f^{(0)}(\boldsymbol{\kappa}, m)}{\partial T}, \tag{A14}$$

which upon simplification takes the form expressed in Eq. (A6) for a wavenumber at a given direction. Thus the heat capacity for a mode per unit volume is

$$c(\boldsymbol{\kappa}, m) = \frac{\hbar\omega(\boldsymbol{\kappa}, m)}{V}\frac{\partial f^{(0)}(\boldsymbol{\kappa}, m)}{\partial T}, \tag{A15}$$

and, by extension, the volumetric heat capacity of the system in phonon space is

$$c_{\text{sys}} = \frac{1}{V}\sum_{m=1}^{3N}\sum_{\boldsymbol{\kappa}} \hbar\omega(\boldsymbol{\kappa}, m)\frac{\partial f^{(0)}(\boldsymbol{\kappa}, m)}{\partial T}, \tag{A16}$$

where the first summation is over $3N$ because the total number of modes at a given wave vector $\boldsymbol{\kappa}$ is equal to the total number of DOF in the system. The c_{sys} quantity is formulated by incorporating the contributions of all modes in the system, including the modes exhibiting localized motion in the nanopillar portion(s). This is because the totality of modes directly corresponds to the totality of DOF of the contiguous integrated internal structure comprising both the membrane and nanopillar portions.

Another important quantity that is defined in phonon space is the local heat flux density vector $\boldsymbol{j}$ which has been related to the temperature gradient in Eq. (A4). The statistical mechanics definition of $\boldsymbol{j}$ is

$$\boldsymbol{j} = \frac{1}{V}\sum_{m}\sum_{\boldsymbol{\kappa}} \hbar\omega(\boldsymbol{\kappa}, m) f(\boldsymbol{\kappa}, m)\boldsymbol{v}_{\mathbf{g}}(\boldsymbol{\kappa}, m), \tag{A17}$$

where f is the phonon distribution function and $\boldsymbol{v}_{\mathbf{g}}$ is the group velocity vector. Similar to Eq. (A16), this quantity is also formulated by incorporating the contributions of all modes in the system, including both phonon and vibron modes. Under the relaxation-time approximation, Eq. (A17) is written as

$$\boldsymbol{j} = -\sum_{m}\sum_{\boldsymbol{\kappa}} \frac{\hbar\omega}{V}\frac{\partial f^{(0)}}{\partial T}\ \boldsymbol{v}_{\mathbf{g}} \otimes \boldsymbol{v}_{\mathbf{g}}\ \tau\ \boldsymbol{\nabla} T, \tag{A18}$$

where, for brevity, the mode-dependency terms $(\boldsymbol{\kappa}, m)$ for ω, $f^{(0)}$, $\boldsymbol{v}_{\mathbf{g}}$, and τ are dropped, and in preparation for the next step, V has been inserted inside the summations. Substituting Eqs (A15) into Eq. (A18) gives

$$\boldsymbol{j} = -\sum_{m}\sum_{\boldsymbol{\kappa}} c\ \boldsymbol{v}_{\mathbf{g}} \otimes \boldsymbol{v}_{\mathbf{g}}\ \tau\ \boldsymbol{\nabla} T. \tag{A19}$$

In the above formulations, the total volume of the NPM (incorporating both the base membrane and nanopillar portions) is used to obtain valid expressions for the volumetric heat capacity in real [Eq. (A11)] and phonon [Eq. (A16)] space and for the heat flux density in phonon space [Eq. (A19)]. Thus the definition of $V = V_{\text{Base}} + V_{\text{Pillar}}$ (where V_{Base} and V_{Pillar} denote the volume of the base membrane and nanopillar portions, respectively) is necessary for satisfying the thermodynamic balance laws inherent in the thermal conductivity prediction models described by each of Eqs. ((A1), (A4), and (A5).

Appendix B: Analysis of the *compensatory effect* in NPM upscaling

A pivotal quantity in our analysis of size and geometric effects in Section IV is the ratio of pillar-to-membrane DOF:

$$V_{\text{r}} = \frac{\text{DOF}_{\text{Pillar}}}{\text{DOF}_{\text{Base}}}. \tag{B1}$$

For our all-silicon NPM unit cell, this quantity is equal to the volumetric ratio mathematically defined as

$$V_{\text{r}} = \frac{\text{V}_{\text{Pillar}}}{\text{V}_{\text{Base}}} = \frac{b \times b \times (h_{\text{T}} + h_{\text{B}})}{aA_x \times aA_y \times d}. \tag{B2}$$

Also of importance is the derivative of this quantity with respect to α,

$$\gamma = \frac{\text{d}\, V_{\text{r}}}{\text{d}\alpha}, \tag{B3}$$

which quantifies the strength of the compensatory effect, i.e., the rate by which the nanopillar(s) size grows compared to the base membrane as the overall unit-cell size is increased. This effect is introduced and utilized in Section IV. The filling fraction of the nanopillar(s) with respect to the area of the surfaces of the base membrane (per unit cell) is defined as

$$A_{\mathrm{r}} = \frac{[b \times b]_{\mathrm{T}}}{[aA_x \times aA_y]_{\mathrm{T}}} + \frac{[b \times b]_{\mathrm{B}}}{[aA_x \times aA_y]_{\mathrm{B}}}, \qquad \text{(B4)}$$

where we recall the subscripts T and B refer to the top and bottom surface of the membrane, respectively. Only one term is retained for the case of a single-sided pillared membrane. This quantity is beneficial for fabrication planning [68].

The A_{r}, V_{r}, and γ quantities for all the cases considered in Fig. 8 are presented as a function of α in Table B.1. In Fig. 8d in particular, the compensatory effect is taken advantage of and shown to comfortably enable two orders of magnitude reductions in the thermal conductivity. Table B.2 lists the numerical values of k_{r} for all the curves presented in Fig. 8d.

To illustrate the size and compensatory effects shown in Fig. 8, we use EMD simulations and the GK method to plot in Fig. B.1a the thermal conductivity reduction k_{r} as a function of nanopillar height (normalized with respect to the base membrane thickness) for a specific NPM configuration, $6\alpha \times 6\alpha \times d + 4\alpha \times 4\alpha \times h_{\mathrm{T}}$ CC, and considering three sizes: $\alpha = 1$, 2 and 3. For all cases, we observe first a reduction in k_{r} with increase in nanopillar height, which confirms that the cause of the thermal conductivity reduction is not limited to boundary scattering but is also due to the resonance effects. This is consistent with observations in Fig. 8d and in previous studies of NPMs [16,23,39]. We also observe, for all three cases, an eventual leveling of k_{r} with increase in nanopillar height which is due to the saturation of the impact of the resonance hybridizations effect with increase in V_{r} [17]. If we now examine a specific value of h_{T}/d (e.g., $h_{\mathrm{T}}/d = 1$), where V_{r} is constant, we observe that the extent of the thermal conductivity reduction deteriorates with increase in NPM size−which is a characteristic of the system as thoroughly reported in Ref. [17]. On the other hand, if we examine the three data points marked with a cross and joined by a dashed line in Fig. B.1a, we observe that k_{r} does not increase but in fact reduces in value. These three data points represent three different NPM sizes (i.e., three different α values) but with nanopillar heights that grow in size at a higher rate than that of the base membrane as α is increased. The increase in the thermal conductivity reduction (reduction in k_{r}) among these three data points demonstrates the compensatory effect. A consequence of this effect is that the larger the size of the unit cell, the less quickly the performance saturates with increasing nanopiller height. In other words, the rewards of increasing the nanopillar height become more significant for larger sized NPM unit cells. This is observed by comparing the rate of saturation in the $\alpha = 3$ curve versus the $\alpha = 1$ curve in Fig. B.1a. The compensatory effect is further elucidated in Figs. B.1b and B.1c in terms of the changes to the group velocities and in Fig. B.1d in terms of the changes to the mode localizations.

In Fig. B.1b, it is clearly seen that the increase in V_{r} intensifies the concentration of group velocity reductions and thus compensates (when $\gamma = 0$), and in some cases overcomes (when $\gamma > 0$), the deterioration in performance due to increase in size. To provide further insight, we show in Fig. B.1c the frequency distribution (from 0 to 1 THz) of the cumulative nonvolumetric thermal conductivity K_{l} of an NPM divided by the same quantity for a corresponding uniform membrane, obtained by the BTE-SMRT technique. The numerator and denominator quantities are obtained by evaluating the integrals $\int_0^{\omega} K_{\mathrm{NPM}}(\omega')d\omega'$ and $\int_0^{\omega} K_{\mathrm{Memb}}(\omega')d\omega'$, respectively. The normalized quantity, $K_{\mathrm{r}}^{\mathrm{Cum}}$, is plotted for each of the three data points considered in Fig. B.1b. Membrane and bulk scattering constants (see Table A.2) are used in the left and right subfigures, respectively. And as a reference, vertical lines are included to represent the total thermal conductivity reduction values obtained by EMD simulations and the GK method.[69] We observe that the compensatory effect takes hold rather strongly within the plotted low-frequency range. The effect takes place throughout the rest of the spectrum as well, but it weakens at higher frequencies and hence the small, yet still negative-slope, change in the total k_{r} value among the three data points as α increases.

The compensatory effect manifests itself also in the changes that take place in the nanopillar-generated mode localizations, as demonstrated in Fig. B.1d. Here we quantify the mode-localization phenomenon by computing the mode participation ratio p_{r}, which is defined for a mode at wave vector $\boldsymbol{\kappa}$ and branch number m by [70,23]

$$p_{\mathrm{r}}(\boldsymbol{\kappa}, m) = \frac{1}{N \sum_{i=1}^{N} [\sum_{j=1}^{3} \boldsymbol{\phi}_{ij}^{*}(\boldsymbol{\kappa}, m) \boldsymbol{\phi}_{ij}(\boldsymbol{\kappa}, m)]^2}, \qquad \text{(B5)}$$

where $\boldsymbol{\phi}_{ij}(\boldsymbol{\kappa}, m)$ is the displacement component corresponding to atom i and direction j of the normalized mode shape. The first summation is over the total number of atoms N in the system, which in our LD calculations consists of a single unit cell (i.e., $N = N_{\mathrm{Base}} + N_{\mathrm{Pillar}}$) and the second summation is over the three directions of motion per atom. The factor p_{r} indicates the degree of localization over the entire system without being specific to a particular region, e.g., the nanopillar or base membrane portion of the unit cell. In Section II, we use the mode weight factor to investigate the degree of regional localization [30–32].

It is clearly observed in Fig. B.1d that most of the p_{r} values for the NPMs are significantly lower than those for the corresponding uniform membranes−this is due to the high mode localizations that take place within the nanopillars, as illustrated in Fig. 2. As discussed earlier,

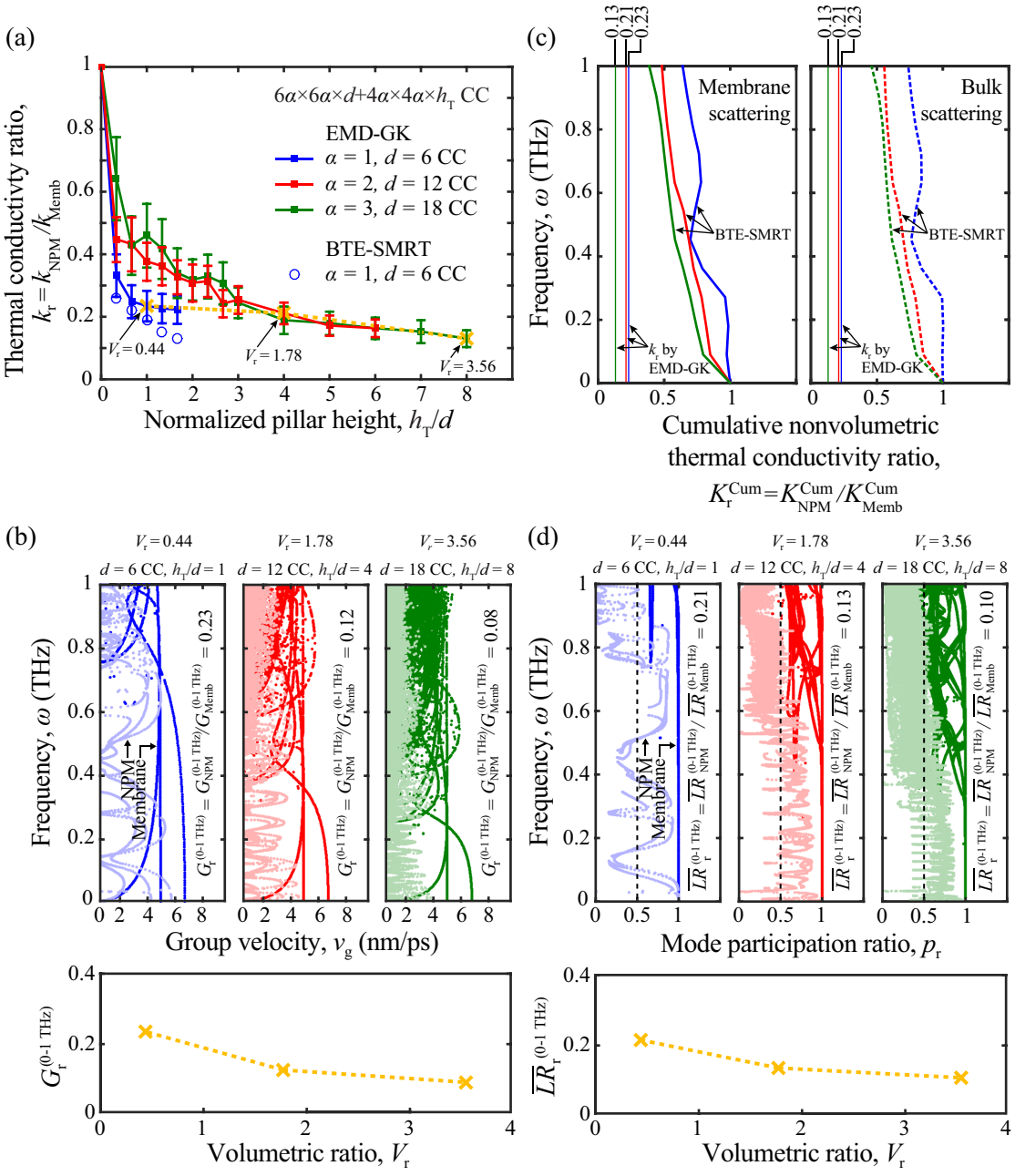

FIG. B.1. (a) Thermal conductivity reduction versus normalized nanopillar height for NPMs of three different sizes. The compensatory effect is evident by comparing the three data points marked with a cross and linked with a dashed line. (b) Group velocity frequency distribution for these data points demonstrating the contrast between uniform and pillared membranes and the increased intensity of the group velocity reductions due to the compensatory effect. (c) Frequency distributions of the cumulative nonvolumetric thermal conductivity ratio K_r^{Cum} for the same data points demonstrating the strength of the compensatory effect at the 0-1 THz frequency range. This quantity, which is obtained using LD and the BTE-SMRT technique, is predominantly influenced by the changes that occur to the group velocities. The thermal conductivity ratios k_r obtained from the EMD-GK method are plotted for comparison. The k_r values are based on the total volume V and therefore account for both the group velocity reductions and the mode localization effect. (d) Mode participation ratios for the same data points demonstrating the contrast between uniform and pillared membranes and the decrease in the delocalization ratio due to the compensatory effect.

Unit cell (CC)	A_r	V_r	$\gamma = dV_r/d\alpha$
Fig. 8a			
$6\alpha \times 6\alpha \times 18 + 4\alpha \times 4\alpha \times 18$	$4/9$	$4/9$	0
$6\alpha \times 6\alpha \times 18 + (6\alpha-2) \times (6\alpha-2) \times 18$	$(1-1/3\alpha)^2$	$(1-1/3\alpha)^2$	$(2/3\alpha^2)(1-1/3\alpha)$
$6\alpha \times 6\alpha \times 18 + 4\alpha \times 4\alpha \times 18\alpha$	$4/9$	$4/9\alpha$	$4/9$
$6\alpha \times 6\alpha \times 18 + (6\alpha-2) \times (6\alpha-2) \times 18\alpha$	$(1-1/3\alpha)^2$	$\alpha(1-1/3\alpha)^2$	$(1-1/9\alpha^2)$
Fig. 8b			
$6 \times 6 \times 6\alpha + 4 \times 4 \times 6\alpha$	$4/9$	$4/9$	0
$6\alpha \times 6\alpha \times 6\alpha + 4\alpha \times 4\alpha \times 6\alpha$	$4/9$	$4/9$	0
$6\alpha \times 6\alpha \times 6\alpha + (6\alpha-2) \times (6\alpha-2) \times 6\alpha$	$(1-1/3\alpha)^2$	$(1-1/3\alpha)^2$	$(2/3\alpha^2)(1-1/3\alpha)$
$6\alpha \times 6\alpha \times 6\alpha + 4\alpha \times 4\alpha \times 6\alpha^2$	$4/9$	$4/9\alpha$	$4/9$
$6\alpha \times 6\alpha \times 6\alpha + (6\alpha-2) \times (6\alpha-2) \times 6\alpha^2$	$(1-1/3\alpha)^2$	$\alpha(1-1/3\alpha)^2$	$(1-1/9\alpha^2)$
Fig. 8c			
$12 \times 12 \times 18 + 10 \times 10 \times 18 + 10 \times 10 \times h_B$	$25/18$	$(25/18)(1+h_B/h_T)$	—
Fig. 8d			
$6\alpha \times 6\alpha \times 6\alpha + (6\alpha-2) \times (6\alpha-2) \times 6\alpha\beta$	$(1-1/3\alpha)^2$	$\beta(1-1/3\alpha)^2$	$(2\beta/3\alpha^2)(1-1/3\alpha)$
$6\alpha \times 6\alpha \times 6\alpha + (6\alpha-2) \times (6\alpha-2) \times 6\alpha\beta + (6\alpha-2) \times (6\alpha-2) \times 6\alpha\beta$	$2(1-1/3\alpha)^2$	$2\beta(1-1/3\alpha)^2$	$(4\beta/3\alpha^2)(1-1/3\alpha)$

TABLE B.1. Explicit form of the A_r, V_r, and γ functions for the NPM configurations considered in Fig. 8

Fig. 8d				
Unit cell (CC)	$k_r(\times 10^{-3})$			
	β	α		
		1	2	3
$6\alpha \times 6\alpha \times 6\alpha + (6\alpha-2) \times (6\alpha-2) \times 6\alpha\beta$	20	38.70±7.91	38.16±6.19	33.93±7.02
	30	34.23±7.38	22.43±4.01	21.60±4.62
	60	21.48±4.12	13.51±1.99	13.31±2.53
$6\alpha \times 6\alpha \times 6\alpha + (6\alpha-2) \times (6\alpha-2) \times 6\alpha\beta + (6\alpha-2) \times (6\alpha-2) \times 6\alpha\beta$	20	18.92±3.74	14.41±2.35	14.40±3.11
	30	17.01±3.86	11.02±1.94	10.26±2.15
	60	11.06±3.04	7.74±1.29	7.69±1.67

TABLE B.2. Thermal conductivity reduction values k_r for the NPM configurations considered in Fig. 8d

these mode localizations contribute to the reduction in the thermal conductivity because each localized mode adds to the total heat capacity of the system yet exhibits effectively zero group velocity. To quantify this effect, a localization ratio LR is defined as the number of modes for which p_r is less than or equal to 0.5, divided by $n_{\boldsymbol{\kappa}} n_m$ where $n_{\boldsymbol{\kappa}}$ is the number of wave-vector points considered and n_m is the number of dispersion branches considered. Conversely, the delocalization ratio $\overline{LR}$ is defined as the number of modes for which p_r is greater than 0.5, divided by $n_{\boldsymbol{\kappa}} n_m$. Thus the sum of these two quantities is equal to unity, i.e., $LR + \overline{LR} = 1$. A decrease in $\overline{LR}$ implies more localized modes. In analogy to our quantification of a net effect in the group velocities due to the addition of the nanopillars, we consider a normalized delocalization ratio defined as $\overline{LR}_r = \overline{LR}_{NPM}/\overline{LR}_{Memb}$. This metric is evaluated in Fig. B.1d for the low-frequency range of 0-1 THz. Similar to the group velocities, we again see a reduction in $\overline{LR}_r^{(0-1THz)}$ as a function of V_r (considering the same three unit cells marked by crosses in Fig. B.1a). This confirms the existence of the compensatory effect also in the context of the mode localization phenomenon.

Appendix C: Addition of a nanopillar on membrane bottom surface

In Figs. 8c and 8d, we have shown that the addition of a nanopillar, in the unit cell, to the bottom surface of a membrane that already has a nanopillar on the top surface reduces the thermal conductivity further. Here we note that the combination of identical nanopillars (one extending from the top and one extending from the bottom) will not produce a spectrum where each particular nanopillar resonance is duplicated, but instead new resonances/vibrons will emerge−which is a favorable outcome. The emergence of new resonances/vibrons is explained by the fact that the overall dynamics of a double-pillared membrane−where the nanopillars are coupled to

a common base membrane, and as such are indirectly connected to each other—will be different than one where there is only a single nanopillar on one surface and the other surface being free. In other words, if we start with a membrane with a nanopillar standing on one surface, by adding a new nanopillar to the other surface we would be modifying the dynamical properties of a system with already altered inertial and stiffness properties. This is in contrast to the case of adding a nanopillar to only one surface where the default dynamical properties are that of a uniform membrane.

In this section, we again consider a double-pillared silicon NPM and examine more closely the underlying cause of the reduction in k_r as the height of the second (bottom) nanopillar is varied. We focus on changes in k_l along the x-direction. For this purpose, we consider as an example the unit-cell configuration $6\times6\times6+2\times2\times h_T+2\times2\times h_B$ CC, fix $h_T = 6$ CC, and allow h_B to vary from 0 to 6 CC in increments of 1 CC. The values of k_r for each of these cases are obtained by the BTE-SMRT technique and plotted as a function of h_T/h_B in Fig. C.1a. The trend is consistent with that obtained by EMD-GK for the similar analysis shown in Fig. 8c. In comparison, the ratio of the average group velocity of the NPM to that of the corresponding uniform membrane versus h_T/h_B is shown in Fig. C.1b. The quantity G_r is evaluated as in Section II A. The trends in Figs. C.1a and C.1b are clearly highly correlated. Thus we observe a direct link between the extent of the group-velocity reductions and the overall thermal conductivity reductions within the NPM considered [17]. Furthermore, adding one more nanopillar increases the number of the localized modes, which in turn leads to an additional reduction in the thermal conductivity. This is what we expect from the nanostructure-induced resonance hybridizations effect.

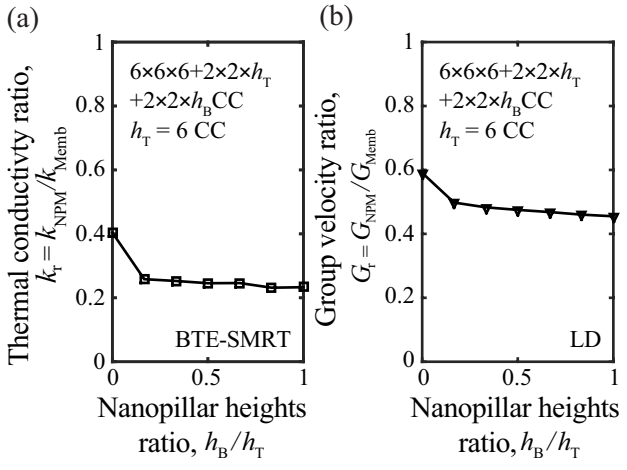

FIG. C.1. (a) Thermal conductivity and (b) average group velocity reduction due to addition of a second (bottom) nanopillar to a membrane unit cell that already has a nanopillar on the top surface. In both subplots, the ordinate is plotted versus the height of the bottom nanopillar, h_B, normalized by the height of the top nanopillar, h_T, which in this analysis is set to 6 CC.

The results of Fig. 8d and Fig. C.1 raise a practical question from a fabrication and device design points of view (see, for example, Ref. [71] which examines the fabrication of silicon nanopillars with high aspect ratios). Which is a better configuration, one with a single tall nanopillar or one with two nanopillars (at the top and at the bottom) where each is half the height of the nanopillar of the first configuration? The answer is given in Table B.2. Comparing, for $\alpha = 3$, the single nanopillar case with $\beta = 60$ to the double nanopillar case with $\beta = 30$ shows that the latter gives a superior performance in reducing the thermal conductivity by roughly 23%.

Appendix D: Multiple thin nanopillars versus single thick nanopillar

In this section, we investigate one more design option for pillared membranes. We compare the performance of a multiple-pillared silicon membrane, where several thin nanopillars are standing on one surface within the unit cell, to an equivalent membrane with only a single nanopillar in the unit cell. In this context, two NPM configurations are considered equivalent if the multiple nanopillars in the first system have the same total number of DOF to that of the single nanopillar in the second system. As an example, we consider a NPM with four nanopillars on the top surface and select the dimensions such that the configuration is equivalent to a $6\times6\times6+2\times2\times6$ CC NPM with a single nanopillar; see Fig. D.1a. The base membrane and the nanopillars have 5,184 and 576 DOF, respectively. For the four-pillared NPM, the nanopillars' heights are denoted h_1, h_2, h_3 and h_4, respectively, the nanopillars are equally spaced at 2 CC, and each nanopillar has a square cross section of 1×1 CC. The four nanopillar heights have a mean value of $\mu = 6$ CC and a standard deviation of σ_s. We choose seven sets as examples, each of which has distinct heights as shown in Table D.1. These sets are sorted in ascending order for the values of σ_s (Set I to Set VII). We compute the thermal conductivity ratio k_r and the average group velocity ratio G_r for these different cases using the BTE-SMRT technique and LD

Set	h_1	h_2	h_3	h_4	σ_s/μ
I	6	6	6	6	0.00
II	4	5	7	8	0.30
III	2	5	8	9	0.53
IV	2	4	6	12	0.72
V	1	2	8	13	0.93
VI	1	3	4	16	1.13
VII	1	2	3	18	1.34

TABLE D.1. Seven sets are considered for the four-pillared NPM shown in the left side of Fig. D.1a, sorted here in ascending order of σ_s/μ. The nanopillars' heights are in units of CC.

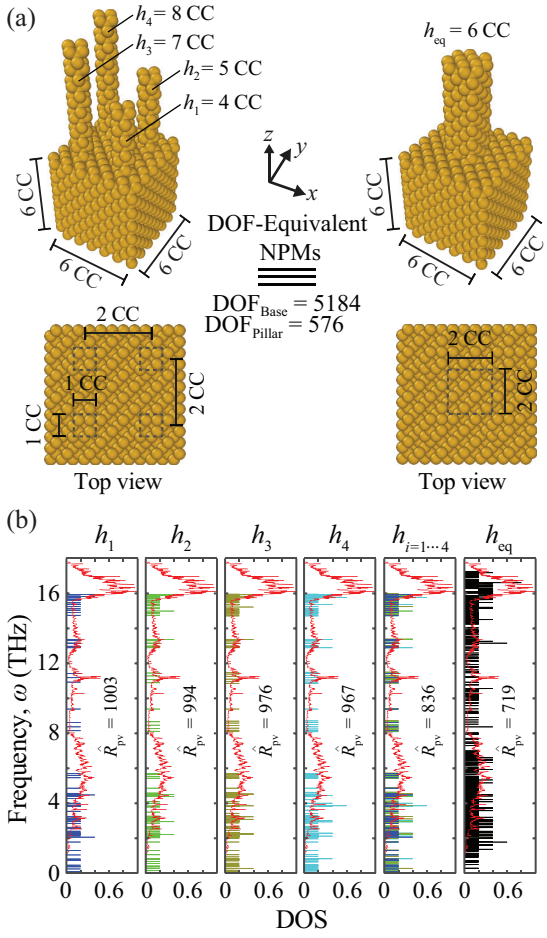

FIG. D.1. (a) Four-pillared NPM compared to (b) an equivalent single-pillared NPM with the same total volume. The mean value of the nanopillar heights is $\mu = 6$ CC. Each nanopillar has a square cross section of 1×1 CC. The equivalent single-pillared NPM has a nanopillar of size 2×2×6 CC. (c) Vibrons DOS for the considered nanopillars where each case is labeled by its height: h_1, h_2, h_3, h_4, or h_{eq}. To allow direct comparison with the vibrons DOS distribution for the thick h_{eq} nanopillar, a superposition of all the vibrons DOS for each of the four thin nanopillars is included and labeled $h_{i=1\cdots4}$. In all these calculations, a nanopillar is examined as an independent nanostructure with free boundary conditions (as done in Figs. 3 and 4). The phonons DOS of the base membrane (without any nanopillars attached) is shown in the foreground in red in all subplots.

calculations, respectively. As shown in Fig. D.2, there is a decreasing trend for each of k_r and G_r as the ratio σ_s/μ is increased. This indicates that a multi-frequency spread emerges that is distinct for each particular combination of the different heights of the nanopillars and its unique vibration resonance distribution. We also compute k_r and G_r for the equivalent single-pillared system (6×6×6 + 2×2×6 CC) and note that it has lower values of each quantity compared to all the four-pillared systems. This indicates that a single-pillared NPM is most likely to be more effective in reducing the thermal conductivity than an equivalent four-pillared NPM with the same

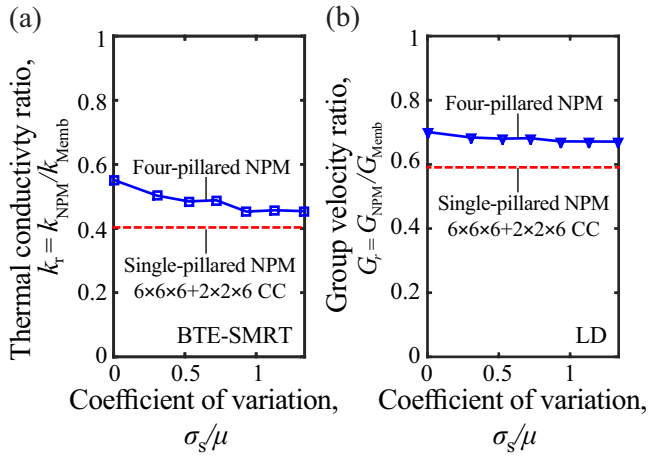

FIG. D.2. (a) Thermal conductivity and (b) average group velocity reduction of the four-pillared NPM and its equivalent single-pillared NPM. The coefficient of variation listed in Table D.1 forms the horizontal axis.

total number of vibrons. For a better understanding of this comparison, the vibrons DOS of each of the four thin nanopillars and the equivalent thick nanopillar are shown in Fig. D.1b. It is clear that the equivalent thick nanopillar has a broader and more phonon-conforming vibrons distribution than the combination of the four single nanopillars ($\hat{R}_{pv}$ for the h_{eq} case is 14% lower than the $h_{i=1\cdots4}$ case). Thus the analysis shown in Fig. 3, where the phonon-vibron correlation is examined for a single nanopillar with various dimensions, is an effective approach for designing a high performing NPM unit cell for thermal conductivity reduction. The structure in the left side of Fig. D.1a, on the other hand, features a sharpened multi-band distribution of vibrons—which we envisage to be useful for applications that require acute *phonon filtering* across certain regions in the frequency spectrum.[72]

Appendix E: Replacement of nanopillars by nanowalls

As mentioned in Section I, the resonating substructures in an NPM may take a variety of forms. An alternative to nanopillars is the introduction of nanowalls with a finite thickness along one direction along the plane of membrane and extended to infinite in the orthogonal direction. A schematic of this modified NPM configuration is shown in Fig. E.1a where a nanowall extends along the full length of the periodic unit cell in the x-direction and has a specified thickness along the y-direction. Compared to a squared nanopillar with the same thickness as the nanowall, the latter has more DOF, thus the NPM exhibits a higher value of V_r and is therefore expected to have a lower value of k_r. Furthermore, the asymmetry of the nanoresonator is expected to produce anisotropic phonon properties and anisotropic planar thermal con-

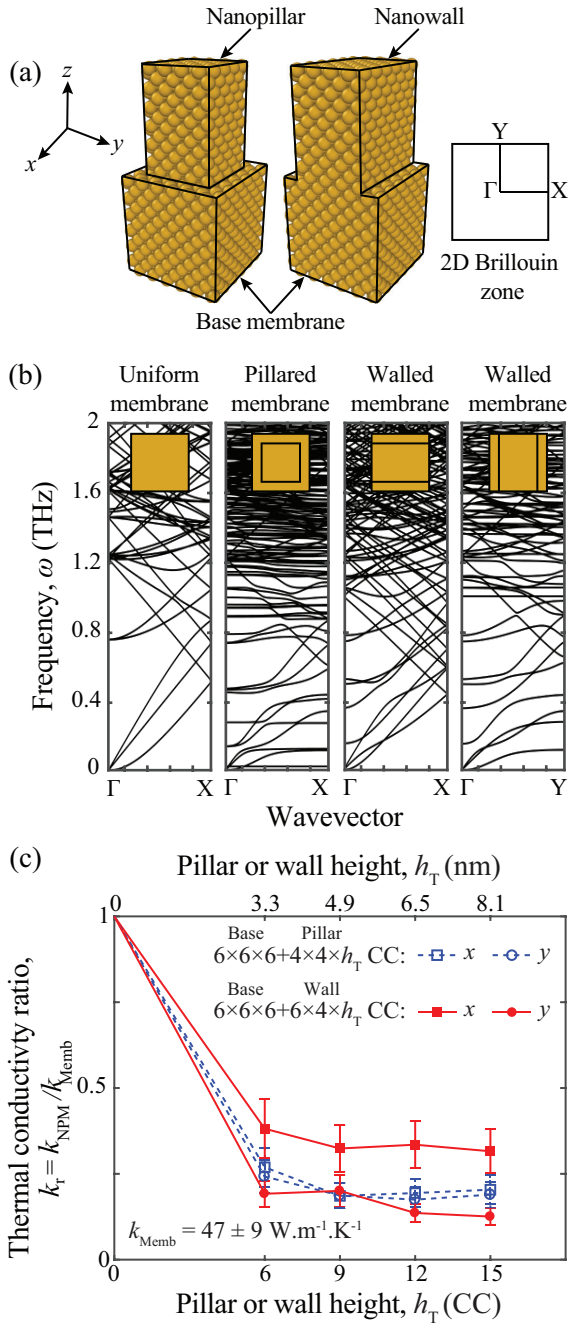

FIG. E.1. (a) Nanowalled membrane versus nanopillared membrane. (b) Phonon dispersions of uniform, pillared, and walled membranes. (c) Thermal conductivity along the x- and y-directions for pillared and walled membranes. The anisotropy in the planar thermal conductivity is evident for walled membranes.

ductivity.

To confirm and quantify these expected results, we investigate a nanowalled membrane with dimentions 6×6×6 + 6×4×6 CC and a corresponding nanopillared membrane with dimensions 6×6×6 + 4×4×6 CC. The nanowall on top of the membrane has the same length as the unit cell along the x-direction and it therefore an extended structure in this direction due to the application of the periodic boundary conditions. Along the y-direction, both the nanowall and nanopillar have the same thickness. In Fig. E.1b, the dispersion curves for a uniform, a nanopillared, and a nanowalled membrane are shown; for the nanowalled case, dispersion diagrams are shown for wave propagation along both the ΓX and ΓY directions. We observe, the ΓX dispersion diagram is highly similar to that of a uniform membrane; indeed there is no periodicity in that direction and the walled membrane is in fact a uniform waveguide along the x-direction. The ΓY dispersion diagram, on the other hand, is comparable to the pillared case because the nanowalls form a periodic system with freely substructures that exhibit a wide range of the resonance modes.

In Fig. E.1, the ΓX and ΓY thermal conductivities of the walled membrane are computed using the EMD-GK method and compared to the pillared case. A total of six simulations were run for each case. It is clear that the pillared membrane is practically isotropic with respect to the x- and y- directions. The walled membrane, on the other hand, displays two distinct values of the thermal conductivity. In the x-direction, the thermal conductivity of the walled system is noticeably smaller than the pillared case and reduces with increasing nanowall height (following a similar saturating trend as for pillared membrane). For a nanoresonator height of $h_T = 15$ CC, we predict an average k_r value of 0.1966 ± 0.0572 for the two pillared cases, and k_r values of 0.3157 ± 0.06368 and 0.1255 ± 0.0255 for the ΓX and ΓY walled cases, respectively. The additional reduction in the thermal conductivity brought about by the nanowalls is a direct outcome of increasing the volume of the nanoresonator. In summary, replacing the nanopillars by nanowalls is shown (i) to reduce the thermal conductivity significantly (by a nearly 30% in the present example) and (ii) introduces a sharp planar anisotropy in the thermal conductivity (by nearly a factor of two in the present example). Furhtermore, adopting nanowalls might be advantageous over nanopillars in terms of ease of nanofabrication.

Appendix F: Comparison with bulk amorphous silicon thermal conductivity

To put the significance of the reductions in the thermal conductivity reported in Fig. 8d further in perspective, here we make a comparison with the thermal conductivity of bulk amorphous silicon at room temperature.

A model of bulk amorphous silicon is produced by the melt-quench technique in the framework of EMD [73]. During a 100-ps process, a model of bulk crystalline silicon is melted by increasing the temperature from 300 to 3500 K under an NVT ensemble (constant number of atoms, volume, and temperature). The melted silicon is then quenched back to 300 K at a rate of 1 K/ps. Following this approach, we run six different samples and report the results in Table F.1. The quality of the produced samples is assessed by computing

the radial distribution function which gives the average coordination number, CN. Our calculations produce a CN value around 4.22, which is slightly higher than the experimental value of approximately 4. This is primarily because of the interatomic potential used. As reported by others, the Stilinger-Weber potential overpredicts the average CN [73]. The calculated density of our samples is 2.329 gcm^{-3}, which is practically the density of crystalline silicon.

We note from Table F.1 that there is no significant computational size effect for the unit cells considered. We therefore average the predictions and obtain a thermal conductivity value of $k_\text{l} = 1.42 \pm 0.01$ $\text{Wm}^{-1}\text{K}^{-1}$. This averaged value agrees well with other investigations in the literature on amorphous silicon [73,74]. Upon comparing with the highest performing 9.78-nm thick double-pillared membrane investigated in Fig. 8d, we find that the NPM has a thermal conductivity that is precisely 1.82 ± 0.19 times lower than that of bulk amorphous silicon.

α	$A_{x,y,z}$ (CC)	$aA_{x,y,z}$ (nm)	k_l ($\text{Wm}^{-1}\text{K}^{-1}$)
1	6	3.26	1.39 ± 0.03
2	12	6.52	1.48 ± 0.03
3	18	9.78	1.38 ± 0.03
4	24	13.03	1.40 ± 0.03
5	30	16.29	1.47 ± 0.02
Average	–	–	1.42 ± 0.01

TABLE F.1. Thermal conductivity of bulk amorphous silicon predicted using a unit cell of size $6\alpha \times 6\alpha \times 6\alpha$

* mih@colorado.edu

[1] M. I. Hussein and I. El-Kady, AIP Adv. **1**, 041301 (2011); M. I. Hussein, I. El-Kady, B. W. Li, and J. Sánchez-Dehesa, *ibid.* **4**, 124101 (2014).

[2] M. I. Hussein, M. J. Leamy, and M. Ruzzene, Appl. Mech. Rev. **66**, 040802 (2014).

[3] G. Chen, Int. J. Therm. Sci. **39**, 471 (2000); A. A. Balandin, J. Nanosci. Nanotechnol. **5**, 1015 (2005); N. B. Li, J. Ren, L. Wang, G. Zhang, P. Hanggi, and B. W. Li, Rev. Mod. Phys. **84**, 10451066 (2012); D. G. Cahill, P. V. Braun, G. Chen, D. R. Clarke, S. Fan, K. E. Goodson, P. Keblinski, W. P. King, G. D. Mahan, A. Majumdar, *et al.*, Appl. Phys. Rev. **1**, 011305 (2014); S. Volz, J. Ordonez-Miranda, A. Shchepetov, M. Prunnila, J. Ahopelto, T. Pezeril, G. Vaudel, V. Gusev, P. Ruello, E. M. Weig, *et al.*, Eur. Phys. J. B **89**, 15 (2016).

[4] S. Alaie, D. F. Goettler, M. Su, Z. C. Leseman, C. M. Reinke, and I. El-Kady, Nat. Commun. **6**, 7228 (2015).

[5] The advent of nanofabrication techniques [75] is providing a powerful enabling tool in this search.

[6] C. J. Vineis, A. Shakouri, A. Majumdar, and M. G. Kanatzidis, Adv. Mater. **22**, 3970 (2010); G. Chen, M. Dresselhaus, G. Dresselhaus, J.-P. Fleurial, and T. Caillat, Int. Mater. Rev. **48**, 45 (2013).

[7] D. M. Rowe, *Thermoelectrics Handbook: Macro to Nano* (CRC Press, Boca Raton, Florida, USA, 2005).

[8] W. Liu, X. Yan, G. Chen, and Z. Ren, Nano Energy **1**, 42 (2012); K. Biswas, J. H. He, I. D. Blum, C.-I. Wu, T. P. Hogan, D. N. Seidman, V. P. Dravid, and M. G. Kanatzidis, Nature **489**, 414 (2012).

[9] A. N. Cleland, D. R. Schmidt, and C. S. Yung, Phys. Rev. B **64**, 172301 (2001); A. J. H. McGaughey, M. I. Hussein, E. S. Landry, M. Kaviany, and G. M. Hulbert, *ibid.* **74**, 104304 (2006); M. N. Luckyanova, J. Garg, K. Esfarjani, A. Jandl, M. T. Bulsara, A. J. Schmidt, A. J. Minnich, S. Chen, M. S. Dresselhaus, Z. F. Ren, *et al.*, Science **338**, 936 (2012).

[10] J. Tang, H.-T. Wang, D. H. Lee, M. Fardy, Z. Huo, T. P. Russell, and P. Yang, Nano Lett. **10**, 4279 (2010); Y. P. He, D. Donadio, J. H. Lee, J. C. Grossman, and G. Galli, ACS Nano **5**, 1839 (2011); B. L. Davis and M. I. Hussein, AIP Advances **1**, 041701 (2011); N. Zen, T. A. Puurtinen, T. J. Isotalo, S. Chaudhuri, and I. J. Maasilta, Nat. Commun. **5**, 3435 (2014).

[11] J. K. Yu, S. Mitrovic, D. Tham, J. Varghese, and J. R. Heath, Nat. Nanotechnol. **5**, 718 (2010).

[12] M. R. Wagner, B. Graczykowski, J. S. Reparaz, A. E. Sachat, M. Sledzinska, F. Alzina, and C. M. Sotomayor Torres, Nano letters **16**, 5661 (2016).

[13] A. I. Boukai, Y. Bunimovich, J. Tahir-Kheli, J.-K. Yu, W. A. Goddard III, and J. R. Heath, Nature **451**, 168 (2008).

[14] S. Neogi, S. Reparaz, L. F. C. Pereira, B. Graczykowski, M. R. Wagner, M. Sledzinska, A. Shchepetov, M. Prunnila, J. Ahopelto, C. M. S. Torres, and D. Donadio, ACS Nano **9**, 3820 (2015).

[15] B. L. Davis and M. I. Hussein, Phys. Rev. Lett. **112**, 055505 (2014); M. I. Hussein and B. L. Davis, US Patent 9,417,465 B2 (2016).

[16] H. Honarvar and M. I. Hussein, Phys. Rev. B **93**, 081412(R) (2016).

[17] H. Honarvar, L. Yang, and M. I. Hussein, Appl. Phys. Lett. **108**, 263101 (2016).

[18] J. B. Pendry, A. J. Holden, D. J. Robbins, and W. J. Stewart, IEEE Trans. Microwave Theory Tech. **47**, 2075 (1999); D. R. Smith, W. J. Padilla, D. C. Vier, S. C. Nemat-Nasser, and S. Schultz, Phys. Rev. Lett. **84**, 4184 (2000).

[19] Z. Y. Liu, X. X. Zhang, Y. W. Mao, Y. Y. Zhu, Z. Y. Yang, C. T. Chan, and P. Sheng, Science **289**, 1734 (2000).

[20] Z. Liu, C. T. Chan, and P. Sheng, Phys. Rev B **65**, 165116 (2002); Y. Pennec, B. Djafari-Rouhani, H. Larabi, J. O. Vasseur, and A.-C. Hladky-Hennion, Phys. Rev. B **78**, 104105 (2008); T. T. Wu, Z. G. Huang, T. C. Tsai, and T. C. Wu, Appl. Phys. Lett. **93**, 111902 (2008).

[21] The unique qualitative nature of the phonon-vibron mode shapes brought about by this concept may also be used to impact other condensed matter properties beyond the thermal conductivity.

[22] Another distinction for NPMs compared to locally resonant electromagnetic, acoustic, and elastic metamaterials is that they draw on their unique properties for the func-

tion intended across the full spectrum and not just within the subwavelength regime.
[23] Z. Wei, J. Yang, K. Bi, and Y. Chen, J. Appl. Phys. **118**, 155103 (2015).
[24] A monotonic improvement in performance will take effect with increasing nanoresonator size as long as the characteristic length scales of the unit cell as a whole are within the full span of the phonon mean free path distribution—as the far end of the distribution is approached, scattering mechanisms will dominate and the probability of occurrences of resonance hybridizations will decay as a result.
[25] M. S. Dresselhaus, G. Chen, M. Y. Tang, R. G. Yang, H. Lee, D. Z. Wang, Z. F. Ren, J.-P. Fleurial, and P. Gogna, Adv. Mater. **19**, 1043 (2007).
[26] F. H. Stillinger and T. A. Weber, Phys. Rev. B **31**, 5262 (1985).
[27] M. I. Hussein, Proc. R. Soc. A **465**, 2825 (2009).
[28] P. W. Anderson, Phys. Rev. **109**, 1492 (1958).
[29] L. R. Rabiner and B. Gold, Englewood Cliffs, New Jersey, Prentice-Hall, Inc. (1975).
[30] A. Bodapati, P. K. Schelling, S. R. Phillpot, and P. Keblinski, Physical Review B **74**, 245207 (2006).
[31] M. Hu and D. Poulikakos, Nano letters **12**, 5487 (2012).
[32] L. Zhu and B. Li, Scientific reports **4**, 4917 (2014).
[33] K. Esfarjani, G. Chen, and H. T. Stokes, Phys. Rev. B **84**, 085204 (2011).
[34] J. A. Johnson, A. A. Maznev, J. Cuffe, J. K. Eliason, A. J. Minnich, T. Kehoe, C. M. S. Torres, G. Chen, and K. A. Nelson, Phys. Rev. Lett. **110**, 025901 (2013); A. J. Minnich, *ibid.* **109**, 205901 (2012).
[35] J. A. Thomas, J. E. Turney, R. M. Iutzi, C. H. Amon, and A. J. H. McGaughey, Phys. Rev. B **81**, 081411 (2010).
[36] J. M. Larkin, J. E. Turney, A. D. Massicotte, C. H. Amon, and A. J. H. McGaughey, J. Comput. Theor. Nanos. **11**, 249 (2014).
[37] J. A. Thomas, J. E. Turney, R. M. Iutzi, C. H. Amon, and A. J. H. McGaughey, Phys. Rev. B **91**, 239905 (2015).
[38] The numerical values of the thermal conductivity reduction for all cases considered in Fig. 8d are provided in Table B.2 in Appendix B.
[39] S. Xiong, K. Sääskilahti, Y. A. Kosevich, H. Han, D. Donadio, and S. Volz, Phys. Rev. Lett. **117**, 025503 (2016).
[40] Future research will explore different nanoresonator configurations to reduce the need for occupying a large volume. For example, the nanopillars may be made from a higher atomic density material in order to generate the same number of vibrons using smaller heights; or may be made from a heavier material in order to shift the vibrons DOS to lower frequencies and thus be effective in reducing the thermal conductivity with shorter nanopillars.
[41] J. Dong, O. F. Sankey, and C. W. Myles, Phys. Rev. Lett. **86**, 2361 (2001); M. Christensen, A. B. Abrahamsen, N. B. Christensen, F. Furany, N. H. Andersen, K. Lefmann, J. Andreassons, and C. R. H. Bahl, Nature Mat. **7**, 811 (2008).
[42] We predict k_l of a 19.55-nm thick uniform silicon membrane to be 2.4 ± 0.4 times lower than the bulk form.
[43] The MFP of electrons in bulk silicon at room temperature has been determined experimentally to range, roughly, from 10 nm to 30 nm depending on the level of doping [44]; thus with moderate doping (which is recommended to optimize between S and σ) it is conceivable that a nanostructure with a 20-nm characteristic size would exhibit negligible change in the electrical properties compared to the bulk form.
[44] L. Weber and E. Gmelin, Appl. Phys. A **53**, 136140 (1991).
[45] A. Stranz, J. Kähler, A. Waag, and E. Peiner, J. Electron Mater. **42**, 2381 (2013).
[46] If we assume that the electrical properties also do not change for the best 9.78-nm thick double-nanopillar case, we would obtain a room-temperature ZT value of 4.8 ± 0.6.
[47] Following the same projection procedure, we obtain a ZT value of 1.8 $\pm 0.3 at$T=700K..*J. Towns*, *T. Cockerill*, *M. Dahan*, *I. Foster*, *K. Gaitl*
[48] E. Helfand, Phys. Rev. **119**, 1 (1960); R. Zwanzig, Annu. Rev. Phys. Chem. **16**, 1798 (1965); A. J. C. Ladd, B. Moran, and W. G. Hoover, Phys. Rev. B **34**, 5058 (1986); S. G. Volz and G. Chen, *ibid.* **61**, 2651 (2000); J. Che, T. Çağn, W. Deng, and W. A. Goddard III, J. Chem. Phys. **113**, 6888 (2000); D. McQuarrie, *Statistical Mechanics* (University Science Books, Sausalito, 2000).
[50] A. J. H. McGaughey and M. Kaviany, Int. J. Heat Mass Tran. **47**, 1783 (2004).
[51] P. K. Schelling, S. R. Phillpot, and P. Keblinski, Phys. Rev. B **65**, 144306 (2002).
[52] E. S. Landry, M. I. Hussein, and A. J. H. McGaughey, Phys. Rev. B **77**, 184302 (2008).
[53] S. Plimpton, J. Comput. Phys. **117**, 1 (1995).
[54] D. P. Sellan, E. S. Landry, J. E. Turney, A. J. H. McGaughey, and C. H. Amon, Phys. Rev. B **81**, 214305 (2010).
[55] Y. He, I. Savić, D. Donadio, and G. Galli, Phys. Chem. Chem. Phys. **14**, 16209 (2012).
[56] J. Taylor, *Introduction to error analysis, the study of uncertainties in physical measurements* (1997).
[57] J. V. Goicochea, M. Madrid, and C. Amon, J. Heat Transf. **132**, 012401 (2010); P. Howell, J. Chem. Phys. **137**, 224111 (2012).
[58] A. Tenenbaum, G. Ciccotti, and R. Gallico, Phys. Rev. A **25**, 2778 (1982).
[59] A similar version of Fig. A.2 is featured in Ref. [17]. In this reference, however, the thermal conductivity predictions of the NPM were based on considering the volume of the base membrane only instead of the entire volume of the NPM. Consideration of the base volume only in the calculations is an approximation that has resulted in an overprediction of k_l by roughly 11%.
[60] N. W. Ashcroft and N. D. Mermin, *Solid State Physics* (Saunders College Publishing, Fort Worth, USA, 1976); G. P. Srivastava, *The Physics of Phonons* (Adam Hilger, Bristol, UK, 1990).
[61] J. D. Gale and A. L. Rohl, Mol. Simulat. **29**, 291 (2003).
[62] C. Kittel, *Introduction to Solid State Physics* (Wiley New York, 1976).
[63] P. T. Landsberg, *Thermodynamics and statistical mechanics* (Courier Corporation, 2014).
[64] P. Attard, *Quantum Statistical Mechanics*, 2053-2563 (IOP Publishing, 2015).
[65] A. J. H. McGaughey and M. Kaviany, Physical Review B **69**, 094303 (2004).
[66] J. Cuffe, J. K. Eliason, A. A. Maznev, K. C. Collins, J. A. Johnson, A. Shchepetov, M. Prunnila, J. Ahopelto, C. M. S. Torres, G. Chen, and K. A. Nelson, Phys. Rev. B **91**, 245423 (2015).
[67] M. T. Dove, *Introduction to Lattice Dynamics*, Vol. 4 (Cambridge University Press, 1993).
[68] J.-Y. Choi, T. L. Alford, and C. B. Honsberg, Langmuir **31**, 4018 (2015).

[69] While BTE-SMRT may predict different thermal conductivities than EMD-GK, the predictions of the relative reductions in the thermal conductivity (i.e., k_r) are generally in good agreement (see Ref. [16] and the BTE-SMRT data points in Fig. B.1a).

[70] L. Yang, N. Yang, and B. W. Li, Nano Lett. **14**, 1734 (2014).

[71] K. J. Morton, G. Nieberg, S. Bai, and S. Y. Chou, Nanotechnology **19**, 345301 (2008).

[72] The vibrons DOS distribution of the unit cell shown in the left side of Fig. D.1a is expected to be slightly different than the superimposed distribution shown in the $h_{i=1...4}$ column of Fig. D.1b because of the coupling with the base membrane and the ensuing changes in the dynamical stiffness when all four nanopillars are present in the same unit cell.

[73] A. France-Lanord, E. Blandre, T. Albaret, S. Merabia, D. Lacroix, and K. Termentzidis, J. Phys.-Condens. Mat. **26**, 055011 (2014).

[74] Y. H. Lee, R. Biswas, C. M. Soukoulis, C. Z. Wang, C. T. Chan, and K. M. Ho, Phys. Rev. B **43**, 6573 (1991); J. M. Larkin and A. J. H. McGaughey, Phys. Rev, B **89**, 144303 (2014); Y. He, D. Donadio, and G. Galli, Appl. Phys. Lett. **98**, 144101 (2011).

[75] A. Biswas, I. S. Bayer, A. S. Biris, T. Wang, E. Dervishi, and F. Faupel, Adv. Colloid Interfac. **170**, 2 (2012).